

# ORBITING CIRCUMGALACTIC GAS AS A SIGNATURE OF COSMOLOGICAL ACCRETION

KYLE R. STEWART<sup>1,8</sup>, TOBIAS KAUFMANN<sup>2</sup>, JAMES S. BULLOCK<sup>3,4</sup>, ELIZABETH J. BARTON<sup>3,4</sup>, ARIYEH H. MALLER<sup>5</sup>,  
 JÜRGE DIEMAND<sup>6</sup>, AND JAMES WADSLEY<sup>7</sup>

<sup>1</sup> Jet Propulsion Laboratory, Pasadena, CA 91109, USA

<sup>2</sup> Institute for Astronomy, ETH Zurich, CH-8093 Zurich, Switzerland

<sup>3</sup> Center for Cosmology, Department of Physics and Astronomy, The University of California at Irvine, Irvine, CA 92697, USA

<sup>4</sup> Center for Galaxy Evolution, Department of Physics and Astronomy, The University of California at Irvine, Irvine, CA 92697, USA

<sup>5</sup> Department of Physics, New York City College of Technology, Brooklyn, NY 11201, USA

<sup>6</sup> Institute for Theoretical Physics, University of Zurich, 8057 Zurich, Switzerland

<sup>7</sup> Department of Physics and Astronomy, McMaster University, Main Street West, Hamilton L8S 4M1, Canada

*Received 2011 March 22; accepted 2011 June 8; published 2011 August 10*

## ABSTRACT

We use cosmological smoothed particle hydrodynamic simulations to study the kinematic signatures of cool gas accretion onto a pair of well-resolved galaxy halos. We find that cold-flow streams and gas-rich mergers produce a circumgalactic component of cool gas that generally orbits with high angular momentum about the galaxy halo before falling in to build the disk. This signature of cosmological accretion should be observable using background-object absorption-line studies as features that are offset from the galaxy’s systemic velocity by  $\sim 100 \text{ km s}^{-1}$ . In most cases, the accreted gas co-rotates with the central disk in the form of a warped, extended cold flow disk, such that the observed velocity offset will be in the same direction as galaxy rotation, appearing in sight lines that avoid the galactic poles. This prediction provides a means to observationally distinguish accreted gas from outflow gas: the accreted gas will show large one-sided velocity offsets in absorption-line studies while radial/bi-conical outflows will not (except possibly in special polar projections). Such a signature of rotation has already been seen in studies of intermediate-redshift galaxy-absorber pairs, and we suggest that these observations may be among the first to provide indirect observational evidence for cold accretion onto galactic halos. This cold-mode halo gas typically has  $\sim 3$ – $5$  times more specific angular momentum than the dark matter. The associated cold-mode disk configurations are likely related to extended H I/extended UV disks that are seen around galaxies in the local universe. The fraction of galaxies with extended cold flow disks and associated offset absorption-line gas should decrease around bright galaxies at low redshift as cold-mode accretion dies out.

**Key words:** galaxies: evolution – galaxies: formation – galaxies: halos – methods: numerical – quasars: absorption lines

*Online-only material:* color figures

## 1. INTRODUCTION

Arguably the most substantive change in our theoretical picture of galaxy formation in the last decade has involved the deposition of gas into galaxies. Cosmological simulations set within the lambda cold dark matter (LCDM) framework show that the majority of galactic baryons should be accreted in a “cold mode,” which does not shock heat in the halo prior to building the galaxy itself (Kereš et al. 2005, 2009b; Dekel & Birnboim 2006; Brooks et al. 2009; Dekel et al. 2009; Faucher-Giguere & Keres 2011; Stewart et al. 2011; van de Voort et al. 2011; Faucher-Giguere et al. 2011). This is quite different from the canonical picture where gas first obtains the halo virial temperature and spin before falling in to form an angular-momentum-supported disk (Silk 1977; White & Rees 1978; Barnes & Efstathiou 1987; White & Frenk 1991; Maller & Bullock 2004). Instead, short cooling times prevent the development of a stable shock near the virial radius in halos that are less massive than a critical threshold (Binney 1977; Birnboim & Dekel 2003) and cool gas gets deposited directly into galactic halos.

Previous simulation studies have noted that this gas seems to be rotating with large amounts of angular momentum, which may help explain what happens to the significant potential energy of the infalling cool gas (Kereš et al. 2009b; Kereš

& Hernquist 2009; Agertz et al. 2009; Brook et al. 2011). Here, we study the cold-mode gas and its detectability in detail, demonstrating that this accreted cool gas orbits about the halo before falling in to build the central disk, delivering not just fuel for star formation but also angular momentum to shape the outer galaxy. This angular momentum enables an observable prediction: cosmological accretion should be discernible in halo absorption-line studies as cool components that are offset from the galaxy’s systemic velocity by  $\sim 50$ – $200 \text{ km s}^{-1}$ , co-rotating with the central disk in most cases.

Though the cold-mode accretion prediction seems to be fairly robust and well understood analytically, there remains no smoking-gun observational evidence that cold-mode accretion is actually occurring in nature. It is important to look for such a signature because it is always possible that additional physics not currently included in simulations changes the story. Such a situation is not out of the question, given that the same simulations that are used to predict and characterize cold-mode behavior also significantly overpredict the baryonic mass function of galaxies (Kereš et al. 2009a). In order to reconcile the relatively high level of baryonic deposition into galaxies with a correspondingly small fraction of baryons locked up in galaxies today (Guo et al. 2010; Behroozi et al. 2010), one must appeal to outflows of some kind. Indeed, observations of cool halo gas around galaxies (typically via metal line absorption systems) have emphasized the presence of gas outflows from

<sup>8</sup> NASA Postdoctoral Program Fellow.

galaxies (e.g., Steidel et al. 1996, 2010; Shapley et al. 2003; Martin 2005; Weiner et al. 2009; Rubin et al. 2010).

The clear observational evidence for outflow (rather than inflow) is at least understandable at high redshift; gas accretion at  $z > 2$  is expected to flow along particularly dense filaments that can penetrate into the center of halos, even above the aforementioned critical halo mass. Dense, narrow streams of this kind may result in globally small covering fractions, making them difficult to observe (Faucher-Giguere & Keres 2011; Kimm et al. 2011; Fumagalli et al. 2011). Galaxies at  $z \sim 2$  are also at the peak of cosmological star formation (Hopkins & Beacom 2006); at these epochs, star-formation-driven feedback processes are even more likely to obscure any indicators of gas accretion (though feedback processes will invariably obscure gas accretion signatures at all epochs, to degrees that are largely unknown). Nevertheless, even at moderate redshifts ( $z < 1.5$ ) there are no definitive observational indications of significant cosmological gas accretion into galaxies in the form of cold-mode accretion.

In a companion paper (Stewart et al. 2011), we showed that while the covering fraction of cool accreted material remains relatively high in low-mass halos at moderate redshifts ( $\sim 30\%$ – $50\%$  within  $R < 50$  kpc at  $z \sim 1$ ), the covering fraction of such gas should drop sharply in halos more massive than the critical threshold for sustaining virial shocks ( $M_{\text{vir}} \sim 10^{12} M_{\odot}$ ). In principle, one would like to examine quasar–galaxy (or galaxy–galaxy) pairs over a range of galaxy masses in order to witness the end of the cold flow regime galaxy-by-galaxy. But in order to do this, one must differentiate absorption signals from accreted gas and absorption from gas that has been deposited there from outflows. In this paper, we show that the kinematics of absorbing gas can provide a means to distinguish its class: halo gas from cold-mode accretion generally rotates about the galaxy.

It should not be surprising that cold-mode gas tends to rotate with the disk. This is the primary mode by which disk galaxies are built in simulations (e.g., Dekel et al. 2009). Cold flows and gas-rich mergers not only supply mass to galaxies but also supply their angular momentum. In fact, we find that cool accreted gas tends to have higher and more coherent specific angular momentum than the dark matter in the halo and this is one property that enables an observable kinematic signature.

In the following section we describe our two simulations, each of which tracks the evolution of a Milky Way-size galaxy down to  $z = 0$ , and we detail our method for creating mock absorption sight lines through the simulations. We briefly explore the general properties of the cool gaseous halos of our simulated galaxies in Section 3. In Section 4, we analyze one of the simulated galaxies at a single point in time, detailing a unique observational signature associated with orbiting halo gas, in the form of an extended disk of cool gas that co-rotates with the galaxy. We investigate the statistical significance of this result in Section 5, analyzing both simulations over a broad range in redshift. We compare this co-rotation signature to observations of galaxy–absorber pairs, and discuss the implications of our results in Section 6. We summarize our findings and conclude in Section 7.

## 2. SIMULATIONS AND ANALYSIS

### 2.1. Simulations

Each of our two simulations utilizes a separate set of cosmological initial conditions, tracking the evolution of a Milky

Way-size dark matter halo until  $z = 0$ . Because we primarily investigate the single most massive galaxy in each simulation, we refer to these simulations throughout this paper as “Halo 1” and “Halo 2.” Halo 1 has an active merger history until  $z \sim 1.5$ , but is subsequently quiescent (a dark-matter-only simulation of the same initial conditions was performed at very high resolution in the Via Lactea II simulation of Diemand et al. 2008<sup>9</sup>). In contrast, Halo 2 experiences a relatively quiescent early history, but has a major merger at  $z \sim 0.8$ , and another large merger at  $z \sim 0.2$ . For both simulations, the most massive galaxy has a dark halo virial mass of  $M_{\text{vir}} = 1.4 \times 10^{12} M_{\odot}$  at  $z = 0$ .

We use “zoom-in” multi-mass particle grid initial conditions generated with the GRAFIC-2 package (Bertschinger 2001). A periodic box of 40 co-moving Mpc is used in each simulation to properly account for large-scale tidal torques. Each simulation contains a high-resolution region, limited to a  $\sim 6$  co-moving Mpc cube; in this region, the masses of the simulation particles in the initial conditions are  $(m_{\text{dark}}, m_{\text{gas}}) = (17, 3.7) \times 10^5 M_{\odot}$ .<sup>10</sup>

We adopt the best-fit cosmological parameters of the *Wilkinson Microwave Anisotropy Probe* three-year data release (Spergel et al. 2007):  $\Omega_M = 0.238$ ,  $\Omega_{\Lambda} = 0.762$ ,  $H_0 = 73 \text{ km s}^{-1} \text{ Mpc}^{-1}$ ,  $n_s = 0.951$ , and  $\sigma_8 = 0.74$ .

We use the code GASOLINE (Wadsley et al. 2004), which is a smoothed particle hydrodynamics (SPH) extension of the pure  $N$ -body gravity code PKDGRAV developed by Stadel (2001). We use a gravitational force softening of 332 pc, which evolves co-movingly until  $z = 9$  and remains fixed from  $z = 9$  to the present. The SPH smoothing length adapts to always enclose the 32 nearest gas particles and has the minimum set to 0.05 times the force-softening length. Renderings of the two simulations are shown in the upper (Halo 1) and lower (Halo 2) panels of Figure 1. The panels from left to right show progressively zoomed renderings of the gas density in each simulation at  $z = 2$ .

The code assumes a uniform UV background from quasi-stellar objects, implemented following Haardt & Madau (1996) and F. Haardt (2002, private communication). It includes star formation and Compton and radiative cooling as described in Katz et al. (1996). The code calculates the abundance of neutral hydrogen by assuming an optically thin ideal gas of primordial composition and in ionization equilibrium with the UV background, treating collisional ionization, photoionization, and recombination processes. Rates for collisional ionization from Abel et al. (1997), radiative recombination from Black (1981) and Verner & Ferland (1996) have been used.

In this paper, we focus on cool gas accretion and the possibility of detecting it as quasar absorption systems, which primarily utilize metal lines (Mg II, C IV, O VI, etc.). To correctly produce metal lines in a simulation of this kind requires radiative transfer, metal diffusion, and modeling of local ionizing sources, which are not included here. Since we are only focusing on the qualitative behavior of halo gas, we will instead give results in terms of H I column density, calculated in the optically thin limit, without local sources. For column densities below the Lyman limit ( $2 \times 10^{17} \text{ cm}^{-2}$ ) our computed column densities should be fairly robust. For higher column densities, we expect a full treatment to lead to quantitative, but not qualitative differences. (See Section 3.1 for a quantitative comparison of our covering

<sup>9</sup> The merger history and other data about this halo can be found at <http://www.ucolick.org/~diemand/vl/>.

<sup>10</sup> For comparison, recent simulations by Kereš & Hernquist (2009) and Faucher-Giguere & Keres (2011) have particle masses of  $9 \times 10^4 M_{\odot}$  and  $4 \times 10^4 M_{\odot}$ , respectively.

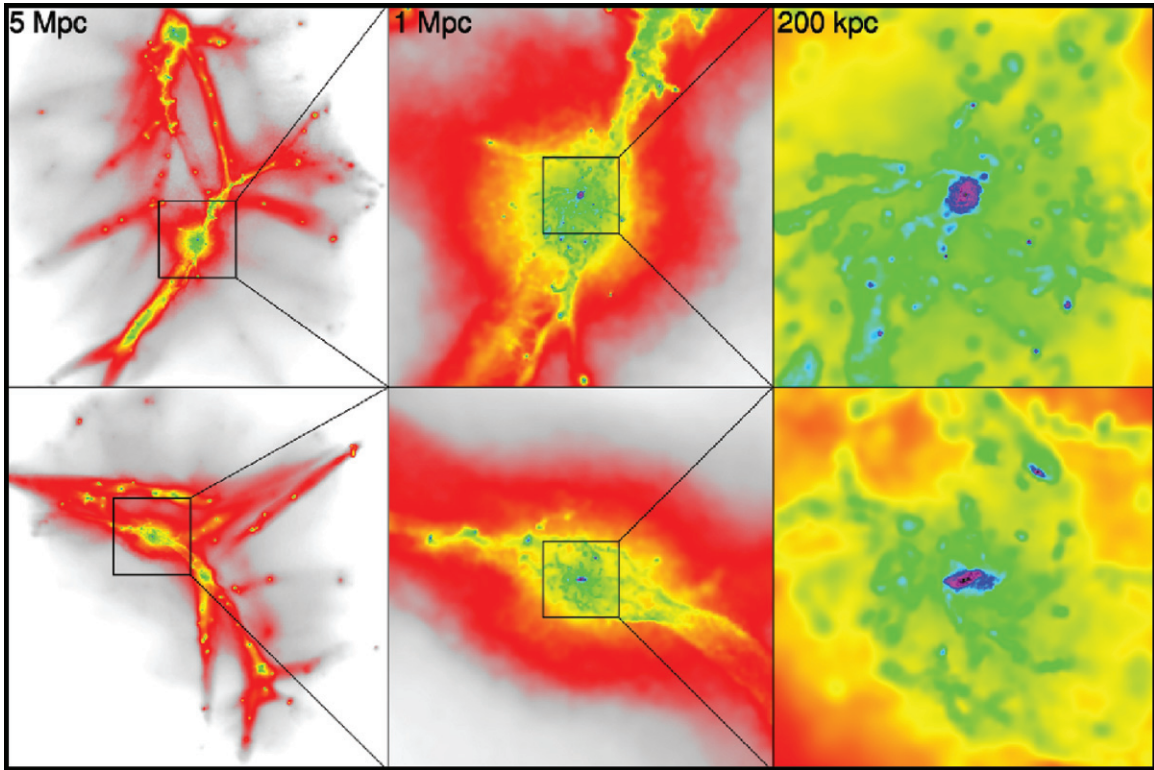


**Figure 1.** Visualization of projected gas density in each of our simulations at  $z = 2$ , with the color variations on a log scale with red, green, and blue corresponding to gas column densities of  $\sim 0.03$ ,  $0.4$ , and  $2.0 M_{\odot} \text{ pc}^{-2}$ , respectively. The top panels show Halo 1 while the bottom panels show Halo 2. From left to right, panel widths correspond to 5 Mpc, 1 Mpc, and 200 kpc in co-moving coordinates. Note that both of our main galaxies reside within an extended filamentary structure at this redshift.

(A color version of this figure is available in the online journal.)

fractions with the recent simulations by Faucher-Giguere & Keres 2011 and Fumagalli et al. 2011 that do contain radiative transfer treatments.)

The “blastwave” supernova feedback model implemented in our simulations creates turbulent motions in nearby gas particles that keeps them from cooling and forming stars, as described in Stinson et al. (2006). The only free parameters in the star formation and feedback model (minimum density threshold,  $\rho_{\text{min}} = 0.1 \text{ cm}^{-3}$ ; star formation efficiency factor,  $c^* = 0.05$ ; and fraction of supernova energy that couples with the interstellar medium,  $\epsilon_{\text{SN}} = 0.1$ ) have been motivated by Governato et al. (2007) in order to produce galaxies with a realistic star formation rates, disk thicknesses, gas turbulence, and Schmidt law over a range in dynamic masses. The feedback model we use here is similar to those used in recent simulations that have shown great success in producing realistic disk-type galaxies (Governato et al. 2009), matching the mass–metallicity relation (Brooks et al. 2007), and matching the abundance of damped Ly $\alpha$  systems at  $z = 3$  (Pontzen et al. 2008). We refer the reader to Governato et al. (2007) for a more detailed description of the simulation code.

With the resolution implemented here, this feedback model results in minimal winds ( $\sim 100 \text{ km s}^{-1}$ ) that mostly affect hot gas, and are more prominent in halos with  $M_{\text{vir}} \lesssim 10^{11} M_{\odot}$  (Shen et al. 2010). Although outflowing gas may be more prominent in higher resolution simulations with higher density thresholds and modified star formation and supernova efficiency parameters (e.g., Governato et al. 2010), we emphasize that the halos discussed here do *not* have outflows of cool gas that would be detectable through absorption.

We define the virial radius for our halos by Bryan & Norman (1998), noting that this is a fairly typical definition used in constructing merger histories from  $N$ -body simulations of dark matter substructure (e.g., Stewart et al. 2008). While this paper primarily focuses on mock observations of absorption lines through our simulated galaxy halos, we analyze the formation and evolution of the galaxies themselves in greater detail in an upcoming paper. Both galaxies are disks before they reach the transition mass for hot-mode accretion ( $M_{\text{vir}} \sim 10^{12} M_{\odot}$ ). After this transition, both galaxies lose their reservoirs of cool high angular momentum halo gas. Halo 1 grows a massive bulge as hot gas cools from the halo, seemingly due to secular instabilities (though it is possible that numerical resolution issues may give rise to artificial bulge creation in the central regions as well). Halo 2 develops into a more spheroidal system due to a major merger just prior to reaching the transition mass. We note that previous works that have produced disk galaxies at  $z = 0$  using a similar code as the one used here typically involve halos less massive than those we study here (e.g.,  $7 \times 10^{11} M_{\odot}$  in Governato et al. 2009), which may be the cause of these morphological differences, since more massive galaxies are known to host a smaller fraction of disk galaxies (e.g., Weinmann et al. 2009).

## 2.2. Mock Absorption Sight Lines

In order to study the kinematics of cool halo gas in a manner useful for comparison to observations, we construct regularly spaced lines of sight around our galaxies for a variety of viewing angles and for different times. For each sight line, we use the analysis software TIPSYS’s “absorb” command to compute the column density of neutral hydrogen per unit velocity, as



a function of velocity along the line of sight, mimicking the practice of searching for absorption gas along a quasar line of sight. The column density is computed by first dividing each sight line into spatial bins of order the size of the spatial resolution of the simulation. For each spatial bin, each gas particle with a smoothing length that intersects the line of sight contributes to the total mass density of the bin. For each of these particles, the contribution of the spline kernel to the column density of each bin that overlaps the kernel is integrated along the line of sight. The velocity of each bin is the mass-weighted velocity of particles contributing to the total column density of neutral hydrogen. Each of these bins is broken into a number of sub-bins, with gas velocity and temperature linearly extrapolated from adjacent bins. Velocity profiles for each sub-bin are based on thermal broadening and dampening wings, with each sub-bin's profile integrated over the velocity bin to determine its contribution.

We limit our examination to absorption lines with  $N_{\text{H I}} > 10^{16} \text{ cm}^{-2}$ , which allows us to focus on the fairly low column densities that our simulations are most capable of reproducing.<sup>11</sup> This range also facilitates our later comparison with weak Mg II absorbing gas, as it is approximately the minimum H I column density associated with Mg II detections (Churchill et al. 2000; Rigby et al. 2002).

Figure 2 shows six example sight lines from our simulations (for Halo 2 at  $z = 1.4$ ) that meet our  $N_{\text{H I}} > 10^{16} \text{ cm}^{-2}$  criterion. In all panels, we plot the column density of neutral hydrogen per velocity bin as a function of velocity, with the galaxy systemic velocity set to 0, represented by the vertical dashed line. In order to compare the kinematics of the absorbing gas to the central galaxy, we classify each line of sight as either *orbiting* or *not orbiting*.

We define a sight line to be *orbiting* if  $>90\%$  of the absorbing gas lies entirely to one side of the systemic velocity of the galaxy, where the galaxy's systemic velocity is the H I-weighted projected velocity through the center of the galaxy. Examples of sight lines classified as orbiting are shown by the left three panels in Figure 2. If this criterion is not met, then we classify the kinematic signature as *not orbiting*. Note that this is a fairly conservative classification, in the sense that we classify even ambiguous cases as not orbiting. In the top right, the classification of *not orbiting* is due to the presence of two distinct components of gas that straddle the systemic velocity (Interestingly, this configuration is reminiscent of something that might be tagged as “outflow” in an empirical study, though in our case, it is simply the chance intersection of two clumps of accreted gas that happen to be orbiting in different directions.) Such a configuration is rare, however; more common examples of gas that is not orbiting are the other right panels, each of which has a single distribution of halo gas near the systemic velocity. In contrast, the left middle panel shows some absorption on both sides of systemic, but because  $>90\%$  of the gas lies to a single side, this sight line is still considered orbiting. This configuration is also rare. Single peaked, relatively narrow absorption lines as shown in the two bottom panels are the

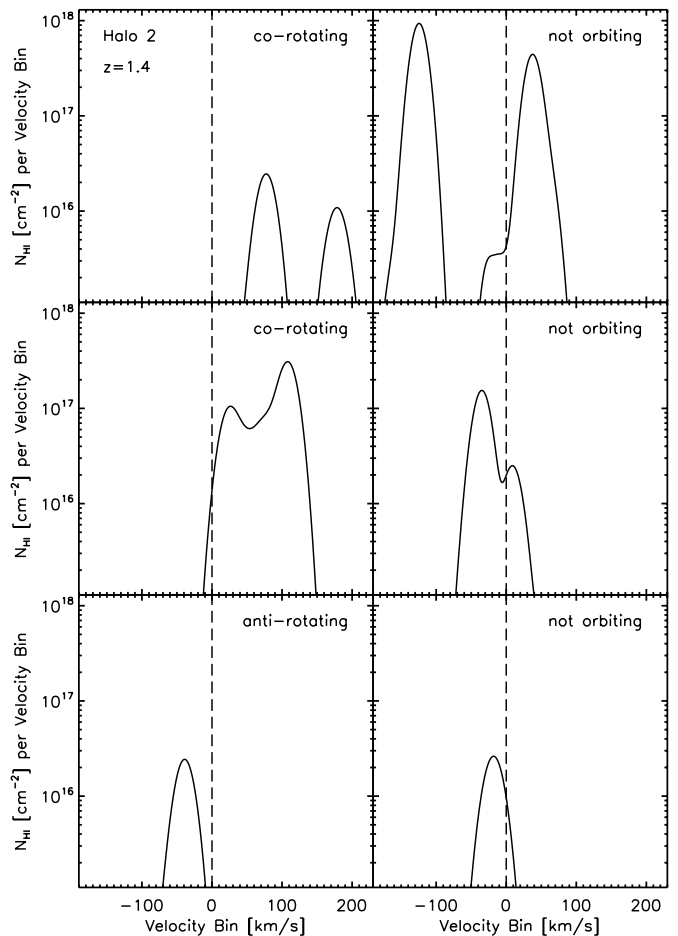


**Figure 2.** Example absorption sight lines taken from Halo 2 at  $z = 1.4$ , showing H I column density per unit velocity vs. line-of-sight velocity. In each panel, the galaxy systemic velocity is  $0 \text{ km s}^{-1}$ , indicated by the vertical dashed line. Left: sight lines that show orbiting gas, with velocity offsets from systemic (see Section 2.2 for definitions). The top and middle plots are co-rotating, due to their spatial positions with respect to the galaxy, while the bottom panel is anti-rotating (i.e., the central galaxy's rotation curve would be positive on this side of the galaxy). The impact parameters of these particular sight lines are (from top to bottom) 50, 20, and 60 co-moving kpc. Right: sight lines that are not orbiting the galaxy, but show velocities near (or on both sides of) systemic. The impact parameters of these sight lines are (top to bottom) 6, 20, and 40 co-moving kpc.

most common profiles, with  $>95\%$  of sight lines having FWHM velocity spreads  $< 110 \text{ km s}^{-1}$ .<sup>12</sup>

We note that in detail orbiting gas may not necessarily show a velocity offset from systemic along an arbitrary projected line of sight. Also, gas that does show a velocity offset from systemic will have unknown radial velocities that could be substantially greater than the velocity offset detected. Despite these shortcomings, we choose to characterize these velocity-offset sight lines as “orbiting” because a full three-dimensional analysis of our galaxies demonstrates that cool halo gas detected by a velocity offset from systemic is typically orbiting the galaxy in a relatively coherent fashion (see Section 4).

If a sight line is found to be orbiting, we further classify it as either *co-rotating* or *anti-rotating* by comparing the direction of the velocity offset with the line-of-sight rotation of the galactic disk along the same projection (sight lines to absorbing

<sup>11</sup> We again emphasize that comparing directly with observed metal lines would require radiative transfer, metal diffusion, and modeling of local ionizing sources, which are not included here. This is why we instead focus on the properties of H I gas at column densities below the Lyman limit ( $2 \times 10^{17} \text{ cm}^{-2}$ ).

<sup>12</sup> Because our feedback model does not produce cool gas outflows, our absorption sight lines are typically within  $500 \text{ km s}^{-1}$  of systemic, and never offset by more than  $1000 \text{ km s}^{-1}$ .

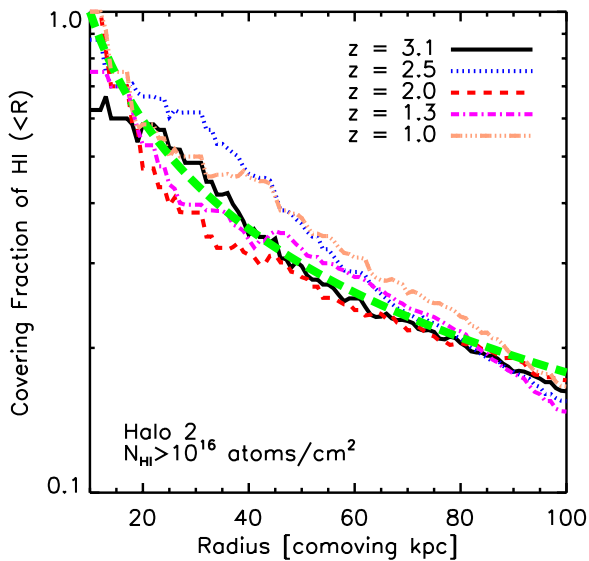


**Figure 3.** Example covering fraction vs. projected radius profiles for Halo 2 at various epochs. The radial profile of  $f_c(<R)$  is similar across a broad redshift range, so long as the galaxy is not experiencing a major merger. The dashed green line shows a power-law fit given by Equation (1).

(A color version of this figure is available in the online journal.)

gas at near right angles to the galactic disk are not included in this classification, as projection effects make these sight lines ambiguous in terms of co-rotation or anti-rotation). As an example, in the left panels of Figure 2, the top and middle panels are co-rotating, due to their projected position with respect to the galaxy, while the bottom left panel is anti-rotating.

### 3. HALO GAS PROPERTIES

Before using our simulated galaxies to probe kinematic signatures of cool halo gas, it is important to know the general properties of our galaxies and their gaseous halos. Because our primary focus is cool halo gas seen in absorption, we choose to first investigate the radial extent of cool gas, to define a useful outer radius within which to focus further analysis.

#### 3.1. Covering Fraction versus Radius

Some past studies of metal line absorption systems associated with galaxies suggest the presence of a critical radius for cool halo gas. In this model, absorption gas extends in a roughly spherical configuration out to a given radius, and gas is unable to cool beyond this radius (e.g., Steidel 1995; Tinker & Chen 2008; Chen & Tinker 2008). Other studies suggest that the covering fraction of detectable absorption systems should decrease as a power law in  $R$  (Martin & Bouché 2009; Steidel et al. 2010).

In order to quantify the radial extent of cool halo gas, we define the *covering fraction* of accreted neutral hydrogen as a function of radius,  $f_c(<R)$ , as the total fraction of sight lines (within a projected radius  $R$  from the center of the galaxy) for which  $N_{\text{HI}} > 10^{16} \text{ cm}^{-2}$  (see Section 2.2 for details on absorption sight line construction). Note that we include the galaxy disk in this analysis, so that  $f_c \sim 1$  for small values of  $R$ . At large radii, this inclusion of the galaxy to the total covering fraction is relatively minor (<10%, 4%, and 1% of sight lines for  $R < 30, 50,$  and  $100$  co-moving kpc, respectively).

Figure 3 shows five example profiles (for Halo 2 at  $z \sim 3, 2, 2.5, 1.3,$  and  $1$ ) of the covering fraction as a function of radius, from  $R < 10$  to  $R < 100$  co-moving kpc, averaged

over three orthogonal orientations of the galaxy, for  $N_{\text{HI}} > 10^{16} \text{ cm}^{-2}$ . Our simulated galaxies do not show a distinct truncation radius that cleanly separates a cold gas regime, but instead we find a smooth progression from higher covering fractions at small radii, to smaller covering fractions at larger radii (though this profile is less smooth during a gas-rich merger). As shown in Figure 3, our  $f_c$  versus  $R$  profiles are quite similar over a wide redshift range. Each curve is well fit by a power law in  $R$ , within the regime  $10 < R < 100$ , with  $R$  in co-moving kpc:

$$f_c(<R) = \left(\frac{R}{R_0}\right)^{-\beta}, \quad (1)$$

where  $R_0$  represents an inner radius within which the covering fraction is  $\sim 100\%$ . The dashed green line in Figure 3 is given by  $R_0 = 10$  co-moving kpc and  $\beta = 0.7$ . We note that our results are in qualitative agreement with Steidel et al. (2010), who found the covering fraction around Lyman-break galaxies at  $z \sim 3$  declines as a power law in  $R$ , with a slope of  $0.2\text{--}0.6$ , very similar to our value of  $0.7$ . In addition, our results are also qualitatively similar to the lower redshift sample ( $z < 0.5$ ) of Chen et al. (2010), who found that the covering fraction is near unity at impact parameters  $R \lesssim 20$  kpc, and declines roughly linearly in  $\log R$  to  $< 5\%$  covering fractions at  $R \sim 100$  kpc.

In detail, the profile we present above also depends on the minimum value of  $N_{\text{HI}}$ , with steeper radial profiles for higher column density gas (similarly, higher equivalents with absorption systems also show steeper radial profiles; see Chen et al. 2010). Accounting for both simulated galaxies, we find more generally that the covering fraction as a function of radius and minimum column density (from  $N_{\text{HI}} \gtrsim 10^{13} \text{ cm}^{-2}$  to  $N_{\text{HI}} \gtrsim 10^{18} \text{ cm}^{-2}$ ) is well fit to the following functional form<sup>13</sup>:

$$f_c(N_{\text{HI}}, <R) = \left(\frac{R}{R_0}\right)^{-\beta(N_{\text{HI}})}, \quad (2)$$

and

$$\beta(N_{\text{HI}}) = \beta_{16} + 0.1 \log[N_{\text{HI}}/10^{16} \text{ cm}^{-2}], \quad (3)$$

with  $R_0 \sim 10$  co-moving kpc and  $\beta_{16} \sim 0.6\text{--}0.8$ . Because the cool gaseous halos of our galaxies die out after cold-mode accretion ends ( $z < 1.3$  and  $z < 0.8$  for Halo 1 and Halo 2, respectively) we caution that this derived fit for  $f_c(<R)$  is based on a narrow halo mass and redshift range:  $M_{\text{vir}} \sim 10^{11}\text{--}10^{12} M_{\odot}$  and  $3 < z < 1$ .

We also caution that our simulations do not have treatment of radiative transfer (see Section 2.2), which may affect the detailed values of  $N_{\text{HI}}$  presented here. In order to give some estimate of how this may impact our resulting covering fractions, we compare the covering fraction of our galaxies at  $z = 2$  with recent high- $z$  simulations of Faucher-Giguere & Keres (2011) and Fumagalli et al. (2011), both of which include post-processing radiative transfer prescriptions for galaxies of similar mass to those analyzed here. At  $z \sim 2$ , those studies both find that  $f_c(< 2R_{\text{vir}}) \sim 4\%$  and  $f_c(< R_{\text{vir}}) \sim 10\%$  for  $N_{\text{HI}} > 10^{17.3} \text{ cm}^{-2}$ , while our simulations (utilizing the above best-fit equation, and  $R_{\text{vir}} \sim 250$  co-moving kpc at  $z = 2$ ) have covering fractions of  $\sim 4\%$  and  $\sim 7\%$ , respectively, for the same column densities.

<sup>13</sup> We note that under the presumption of a power-law form for  $f_c(<R)$ , the *differential* covering fraction of gas *precisely* at the projected radius  $R$  must follow the same power-law slope, with a normalization that is lower by a factor of  $(1 - \beta/2)$ .

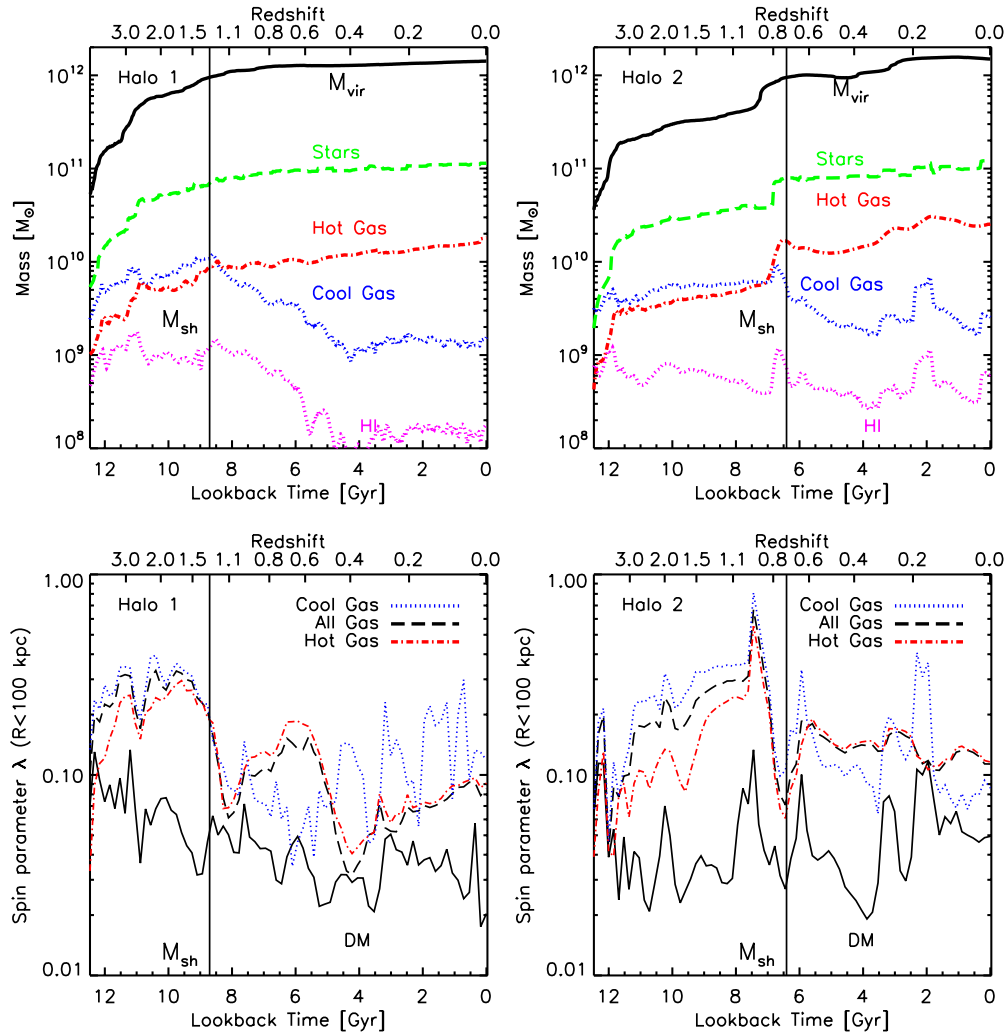


**Figure 4.** Baryonic masses and spin parameters ( $R < 100$  co-moving kpc of each simulated galaxy) vs. time. The left panels show Halo 1, while the right panels show Halo 2. Top: the total mass within the virial radius is shown by the solid black line, while the stellar mass, hot gas mass ( $T > 10^5$  K), cool gas mass ( $T \leq 10^5$  K), and H I gas mass within  $R < 100$  co-moving kpc are given by the dashed green, dot-dashed red, dotted blue, and dotted magenta lines, respectively. Bottom: the spin parameter of the dark matter and gas within  $R < 100$  co-moving kpc (see Equation (4)). The dark matter spin parameter is given by a solid black line, while the spin parameters of cool gas, hot gas, and all gas are given by the blue dotted, red dot-dashed, and black dashed lines, respectively. Note that after rapid accumulation of angular momentum from mergers, the dark matter spin parameter quickly settles to pre-merger values, while the gas spin parameters stay higher considerably longer. The vertical line in each panel shows where the galaxy crosses the transition from cold-mode to hot-mode accretion,  $M_{\text{vir}} = M_{\text{sh}} \sim 10^{12} M_{\odot}$ , as motivated by Dekel & Birnboim (2006) for shocks at a moderately large fraction of the virial radius. After this threshold, little cool gas reaches the galaxy from cold flow accretion.

(A color version of this figure is available in the online journal.)

This indicates that the lack of radiative transfer may lower the available H I content in the halos of our galaxies, suppressing the covering fraction by a factor of  $\sim 30\%$  at a fixed column density threshold. (This, in turn, suggests that our reported column densities may be slightly higher than they would be with inclusion of radiative transfer.) Because the rest of this paper primarily discusses the kinematic properties of cool halo gas in our galaxies, only utilizing the integrated column densities of sight lines to determine if they are potentially observable or not, we do not believe the lack of radiative transfer will substantially alter our findings.

It is worth noting that most of the accreted halo gas resides within  $R < 100$  co-moving kpc of our simulated galaxies, with the only notable exception being major, gas-rich galaxy mergers that have not yet fallen within this radius. (Mergers of this kind are more likely at high redshift, when mergers are more common, and galaxies are more gas rich than at lower redshift; see, e.g., Stewart et al. 2009a, 2009b.) Since the infall time of

major mergers is short (e.g., Boylan-Kolchin et al. 2008), we will focus our analysis on  $R < 100$  co-moving kpc for the remainder of this paper. For our simulated halos, this choice of radius corresponds to  $\sim R_{\text{vir}}/2$  at  $z = 3$  and  $\sim R_{\text{vir}}/3$  at  $z = 0$ .

### 3.2. Mass and Angular Momentum Evolution

The top panels in Figure 4 show the mass buildup of each galaxy over cosmic time, with the left and right panels showing Halo 1 and Halo 2, respectively. In each panel, the solid black line shows the total virial mass of each halo (including dark matter and all baryons within  $R < R_{\text{vir}}$ ), while the other curves represent the baryonic masses within  $R < 100$  co-moving kpc; the dashed green, dot-dashed red, dotted blue, and dotted magenta lines show the stellar mass, hot gas mass ( $T > 10^5$  K), cool gas mass ( $T \leq 10^5$  K), and H I gas mass, respectively.

Once each galaxy crosses the critical halo mass for forming shocks,  $M_{\text{sh}}$ , accreted gas is shock heated strongly enough that very little cool gas reaches the inner halos of our galaxies. This

point is indicated by vertical lines in each panel of Figure 4. We see that after this critical transition, the gas mass in the halo becomes dominated by the hot component (red dot-dashed line) and the cool component drops in comparison (blue dotted line). At the same time, the covering fraction of cool gas drops severely (Stewart et al. 2011) and the galaxies begin to evolve into more bulge-dominated morphologies, rather than disks (see Section 6.3 for more on this transition).

Given that the velocity distribution of halo gas is the key observational signature we are exploring, it is useful to characterize the kinematics of orbiting halo gas in terms of its angular momentum. A useful way to do this is via a dissipationless spin parameter (Peebles 1969). Specifically, we compare the specific angular momentum  $j$  of the dark matter, hot gas, and cool gas as a function of time in each halo using the spin parameter defined by Bullock et al. (2001):

$$\lambda_x \equiv \frac{j_x}{\sqrt{2} V R}. \quad (4)$$

Here,  $j_x$  is the specific angular momentum of component  $x$  (= dark matter, hot gas, cool gas, and all gas) within a sphere of radius  $R$  and  $V$  is the circular velocity measured at radius  $R$ .

The bottom panels of Figure 4 show the spin parameter for the dark matter within  $R = 100$  co-moving kpc as a solid black line. The spin parameter evolution of the gaseous components within the same radius is represented by the black dashed (all gas), blue dotted (cool gas), and red dot-dashed lines (hot gas). Note that the spin parameter in dark matter evolves somewhat stochastically, spinning up in response to mergers (Vitvitska et al. 2002; Maller et al. 2002) but then settling down as the halos re-virialize and the angular momentum is redistributed (D’Onghia & Navarro 2007). The redistribution does not happen as readily in gas, which tends to cohere and spin up more strongly. The average spin for the dark matter bounces around  $\lambda_{\text{dm}} \sim 0.04$  over time, at a value that is quite similar to the expectations of many past studies from dissipationless simulations (recently, Bett et al. 2007, 2010; Macciò et al. 2007; Berta et al. 2008). On the other hand, the gaseous halo components have much more angular momentum, demonstrating a more sustained response to mergers and inflow. The cool gas has the highest spin of all, some  $\sim 3$ – $5$  times higher than that of the dark matter with  $\lambda_{\text{coolgas}} \sim 0.1$ – $0.2$ . We emphasize that this result is particularly important for theoretical studies that try to understand angular-momentum-supported disk sizes. There is a long history of studies relying on spin parameter distributions derived from dissipationless simulations to predict disk sizes and bulge properties in galaxies (e.g., Fall & Efstathiou 1980; Blumenthal et al. 1986; Mo et al. 1998; Bullock et al. 2001). Given that cool halo gas is the primary component that actually builds galaxies (e.g., Dekel et al. 2009), our result that  $\lambda_{\text{coolgas}} \sim 4 \lambda_{\text{dm}}$  motivates reconsideration of the issue of disk sizes in a cosmological context (see also Maller & Dekel 2002).

Before moving on, we note that while we have included disk gas and halo gas in our  $\lambda$  determinations, the gas associated with the central disk typically constitutes only  $\sim 10\%$ – $20\%$  of gas within this radius, and is therefore unimportant to the quantities plotted here. That is, the spin parameters we are discussing are dominated by *halo gas*. We will present a more detailed study of the angular momentum buildup of these galaxies in an upcoming paper.

The relatively large amount of angular momentum in the cool component suggests that cold-accretion material may display

a smoking-gun signature in its kinematics. In the following section we demonstrate not only that this gas is rapidly orbiting about the halo center, but that it tends to rotate *with* the central disk. This is not surprising given that this is the gas that fuels disk formation in the end. What is important for our purposes is that this co-rotation between cool halo gas and the galaxy disk can be observed via halo absorption studies.

## 4. KINEMATICS OF COOL HALO GAS

### 4.1. Co-rotation of Cool Accreted Halo Gas

The kinematics of cool gas in the halos of galaxies serve as an important probe of galaxy formation. Unfortunately, the detailed nature of cool halo gas is difficult to determine empirically, as observations are presently limited to studying absorption along quasar lines of sight. As a result, even when the resulting sight line is close enough to a foreground galaxy to probe its gaseous halo, these observations only allow for a single absorption line of sight per galaxy. Fundamental properties such as the covering fraction and kinematics of cool halo gas can only be accumulated in a statistical manner, for many different galaxies, with varied properties, redshifts, and distances between the absorbing gas and the galaxy. Despite these inherent difficulties, observations of cool halo gas have progressed substantially in the past decade—typically utilizing Mg II absorption, which arises in low-ionization, metal-enriched gas of fairly high density and probes neutral hydrogen column densities of  $\sim 10^{16}$ – $10^{22}$  cm $^{-2}$  (Rigby et al. 2002; Churchill et al. 2000).

Still, it remains unclear what fundamental processes give rise to the absorbing gas. Different observations suggest that it may result from extended thick disks (Steidel et al. 2002), cool cloud formation from hot halo gas (Chen & Tinker 2008), cool gas that is outflowing from galaxy-scale winds (Bond et al. 2001; Bouché et al. 2006; Prochter et al. 2006; Weiner et al. 2009; Steidel et al. 2010; Rubin et al. 2011), tidal streams from recent merger activity (Churchill et al. 2005; Rubin et al. 2010), or a complex combination of the above, with inclusion of cosmological gas accretion along filaments (Kacprzak et al. 2007, 2010). In this section, we create mock observations of our simulated galaxies, utilizing line-of-sight absorption profiles of cool gas (as detailed in Section 2.2) to probe observable kinematic signatures of cool accreted gas.

Before analyzing our mock absorption lines, we give a visual impression of the rotation of cool gas within  $R < 100$  co-moving kpc in Figure 5. For each pixel in the image, the blue–red shading corresponds to the mass-weighted average velocity of H I gas along the line of sight. The galaxy, seen near edge-on in the inner region of the figure (at an inclination of  $75^\circ$ ), shows a clear rotation signature; gas on the left side of the disk shows a negative (blue) line-of-sight velocity while the right side of the disk has a positive (red) line-of-sight velocity. As shown, the rotation signature extends well beyond the galactic disk; in fact, the *majority* of cool halo gas out to  $R < 100$  co-moving kpc is co-rotating with the galaxy.

This kinematic correlation is not surprising, given that the angular momentum vectors of the inner and outer regions of dark matter halos are expected to be in rough alignment (typical misalignment  $\sim 30^\circ$ ; e.g., van den Bosch et al. 2002; Sharma & Steinmetz 2005; Bailin et al. 2005; Bett et al. 2010). Nor is it surprising that cold-mode gas has high angular momentum before falling in to build the disk, as multiple past investigations into the properties of cold-mode accretion have noted the presence of high angular momentum cool gas in proximity



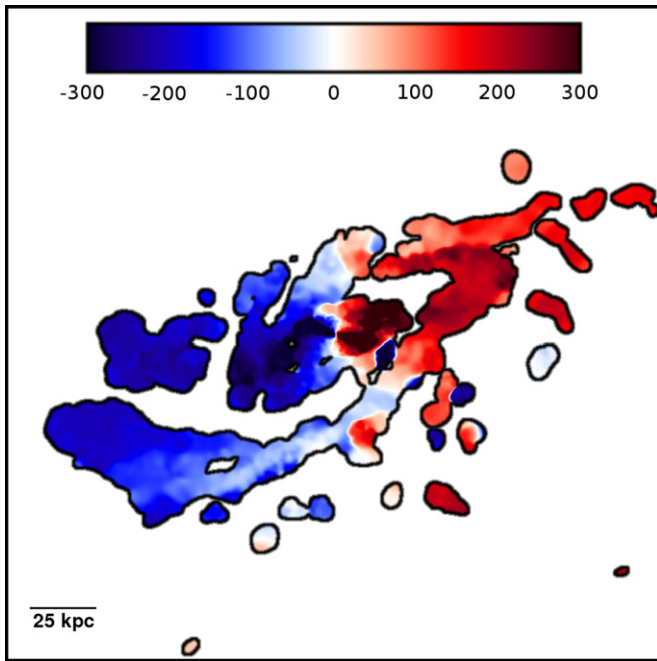


**Figure 5.** Line-of-sight velocity of cool halo gas in Halo 2's main galaxy at  $z = 1.4$ . The image width is 200 co-moving kpc, and the galaxy is viewed near edge-on at an inclination of  $75^\circ$ . The black contours enclose regions with  $N_{\text{HI}} > 10^{16} \text{ cm}^{-2}$ , and the blue–red shading shows the average (mass-weighted) velocity of H I along the line of sight, from  $-300$  to  $300 \text{ km s}^{-1}$ . The galaxy (inner region) tends to rotate in the same direction as cool halo gas, even out to 100 co-moving kpc.

(A color version of this figure is available in the online journal.)

to (but more extended than) the galaxy (Kereš et al. 2009b; Kereš & Hernquist 2009; Agertz et al. 2009; Brook et al. 2011). Indeed, the gravitational potential energy of infalling gas should result in velocities of  $\sim 100\text{--}300 \text{ km s}^{-1}$ , and if this energy is not dissipated by shock heating, the conversion of potential

energy into rotational velocity is a quite natural possibility (see discussion in Kereš et al. 2005).

While Figure 5 gives an intuitive visual impression of this rotation, a mass weighted velocity of cool gas along a line of sight is not directly observable. In order to determine if this co-rotation signature might be observed via studies of absorption systems, we analyze 794 regularly spaced absorption profile sight lines within  $R < 100$  co-moving kpc of the central galaxy.<sup>14</sup> Comparing each absorption profile to the rotation signature of the galactic disk, we categorize sight lines as orbiting or not orbiting based on their velocity offsets, and further divide orbiting sight lines into those that are co-rotating or anti-rotating with the galactic disk (see Section 2.2 for detailed definitions of these classifications).

Figure 6 again shows Halo 2 at  $z = 1.4$  (this time viewed edge-on), but presenting a more observationally oriented method than before. For both panels in Figure 6, the image width is 200 co-moving kpc, with the black circle marking a 100 co-moving kpc radius from the center of the galaxy. The colored contours in the background of each panel show the projected column density of H I with the color code on a log scale from  $> 10^{16} \text{ cm}^{-2}$  (red) to  $> 10^{22} \text{ cm}^{-2}$  (purple/black). On this scale, the edge-on disk is visible as the dark horizontal bar across the very center of the image. We remove sight lines in the central region ( $R < 10 \text{ kpc}$ ) from our analysis, since we are interested in the properties of the cool *halo* gas, not gas that is likely associated with the galactic disk. (This is why there are no symbols in the center of either image.) Along this projection, the central galaxy is redshifted on the left and blueshifted on the right.

In the left panel, we have overlaid symbols representing the division between sight lines with significant velocity offsets (orbiting sight lines; filled circles) and those that do not (open squares). As the figure makes clear, the vast majority of sight lines are orbiting about the central galaxy, with velocities offset

<sup>14</sup> The 794 sight lines form a square grid of  $32^2$  cells within a cube of length 200 co-moving kpc per side, after removing cells with  $R \geq 100$  co-moving kpc.

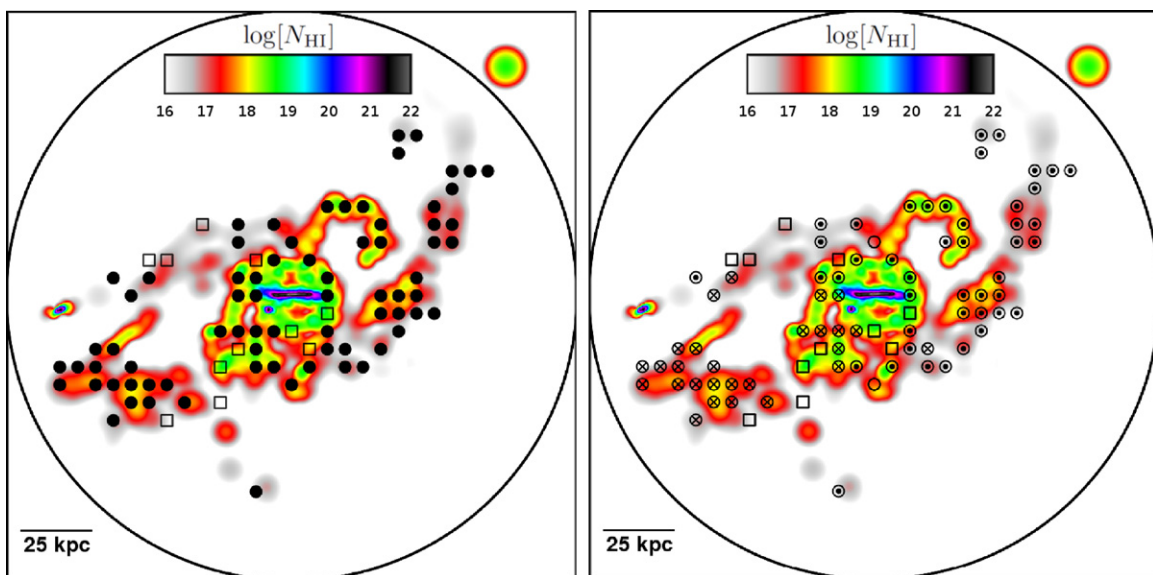


**Figure 6.** Co-rotation of cool halo gas in Halo 2's main galaxy at  $z = 1.4$ . The large black circles denote a radius of 100 co-moving kpc and the logarithmic color scale shows the projected column density of H I. In the left panel, observable sight lines ( $N_{\text{HI}} > 10^{16} \text{ cm}^{-2}$ ) are categorized as orbiting (filled circles) or not orbiting (open squares). In the right panel, the direction of the velocity offset of orbiting sight lines is explicitly displayed, with redshifts and blueshifts given by circle-X and circle-dot symbols, respectively.

(A color version of this figure is available in the online journal.)



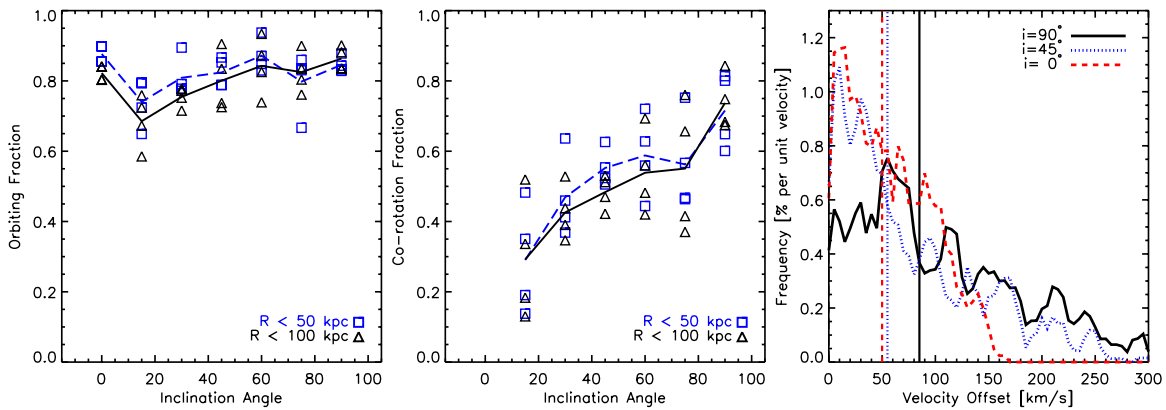


**Figure 7.** Observable characteristics of halo absorption-line kinematics as a function of central galaxy inclination angle for Halo 2 at  $z = 1.4$ . At each angle, we have analyzed four viewing orientations around the galaxy. Left and middle: the orbiting and co-rotation fractions for different galaxy orientations. Squares and triangles show  $R < 50, 100$  co-moving kpc statistics, with each symbol representing a different orientation of the galaxy. The orbiting fraction is universally high, while co-rotation fractions vary strongly with galaxy inclination. Right: magnitude of velocity offset with galaxy inclination. Each curve shows the relative frequency of different velocity offsets for different galaxy inclinations, for lines of sight with  $R < 100$  co-moving kpc and  $N_{\text{H I}} > 10^{16} \text{ cm}^{-2}$ . The vertical lines indicate the median velocity offset for each inclination angle.

(A color version of this figure is available in the online journal.)

from the systemic velocity of the system. At this particular snapshot, the *orbiting fraction* (fraction of all  $N_{\text{H I}} > 10^{16} \text{ cm}^{-2}$  sight lines which are orbiting) is  $\sim 90\%$ .

The right panel is identical to the left, except that orbiting sight lines (filled circles) now have their velocity offset shown explicitly, so that we may determine which are co-rotating or anti-rotating with the galaxy. Sight lines that are redshifted with respect to systemic (“into” the image) are shown by circle-X symbols, while blueshifted sight lines (“out of” the image) are given by circle-dots. For this example snapshot and orientation, co-rotating sight lines follow the kinematics of the galaxy: redshifted on the left side of the image or blueshifted on the right side of the image. The *co-rotation fraction* (fraction of  $N_{\text{H I}} > 10^{16} \text{ cm}^{-2}$  sight lines that show this co-rotation signature) is  $\sim 70\%$  for this image.<sup>15</sup>

#### 4.2. Effects of Galaxy Inclination

In order to investigate the generality of our results, we repeat our kinematic analysis from Section 4.1 for four equally spaced viewing angles around each galaxy (at the same inclination, from  $0^\circ$  to  $135^\circ$ , inclusive) as well as seven equally spaced galaxy inclinations ( $0^\circ$ – $90^\circ$ , inclusive) for a total of 28 unique orientations per galaxy. Continuing with the  $z = 1.4$  snapshot of Halo 2, Figure 7 shows how the orbiting fraction (left panel) co-rotation fraction (middle panel) and velocity-offset distributions (right panel) vary with these different orientations. In the left two panels, the x-axis shows the seven different inclinations of the galaxy, while each of the four symbols along the y-axis shows one of the four different viewing angles around the galaxy.<sup>16</sup> In order to explore how the orbiting and co-rotation fractions might vary with radius, we show statistics for two choices of outer radii (squares and triangles for  $R < 50$  and  $100$  co-moving kpc, respectively). The dashed and solid curves give the mean values at each inclination for  $R < 50$  and  $R < 100$  co-moving kpc, respectively.

Regardless of the galaxy’s orientation, the overall orbiting signature stays constant, with a mean orbiting fraction of  $\sim 70\%$ – $90\%$ . This velocity-offset signature is *not* a strong function of radius from the central galaxy. Cool halo gas at  $R = 100$  co-moving kpc seems equally likely to be orbiting about the galaxy in some fashion as gas that is closer in to the galaxy.

In contrast, the co-rotation fraction varies strongly with the orientation of the galaxy. At a fixed inclination, the co-rotation signature shows scatter of  $\sim 20\%$ – $30\%$ , depending on the viewing angle, but even more drastic is the dependence on inclination. Averaging over the four viewing angles,  $\sim 70\%$  of absorption sight lines appear to be co-rotating with the galaxy when viewed near edge-on. When viewed near face-on, not only does this co-rotation signature drop, but the cool halo gas actually appears to be *anti-rotating*.

The right panel of this figure investigates this issue further, showing the distribution of velocity offsets for different galaxy inclinations (averaged over the four viewing angles). When the galaxy is viewed near edge-on (solid black line), the cool halo gas shows a wide distribution of velocities, with velocity offsets up to  $\sim 300 \text{ km s}^{-1}$  from the galaxy’s systemic velocity, and an average velocity offset of  $\sim 100 \text{ km s}^{-1}$  (the vertical line). While most sight lines still show velocity offsets at higher inclinations (i.e., most sight lines are still orbiting) the *magnitudes* of these offsets are smaller, typically within  $\sim 100 \text{ km s}^{-1}$  from systemic, with an average offset of  $\sim 50 \text{ km s}^{-1}$ . These smaller magnitudes allow for projection effects to grow increasingly important for lines of sight to near face-on galaxies.

In order to fully understand this trend with inclination, Figure 8 presents six different orientations of this galaxy (the same galaxy as Figures 5, 6, and 7: Halo 2 at  $z = 1.4$ ). The contours and symbols in Figure 8 are identical to Figure 6, with the left, middle, and right panels showing the galaxy at inclinations of  $90^\circ$ ,  $45^\circ$ , and  $0^\circ$ , respectively.<sup>17</sup> The top and bottom panels show two different viewing angles around the galaxy ( $90^\circ$  apart).

Apparent in the upper left panel of this figure is that most of the cool halo gas around this galaxy is confined to a single

<sup>15</sup> Since lines of sight perpendicular to the plane of the galaxy cannot be classified as co-rotating or anti-rotating, we leave these as open circles, and do not include them in computation of the co-rotation fraction.

<sup>16</sup> The order of rotation for all 28 orientations is first by angle, then by inclination.

<sup>17</sup> The face-on panels at the right show a “top-down” view of the edge-on panels at the left.

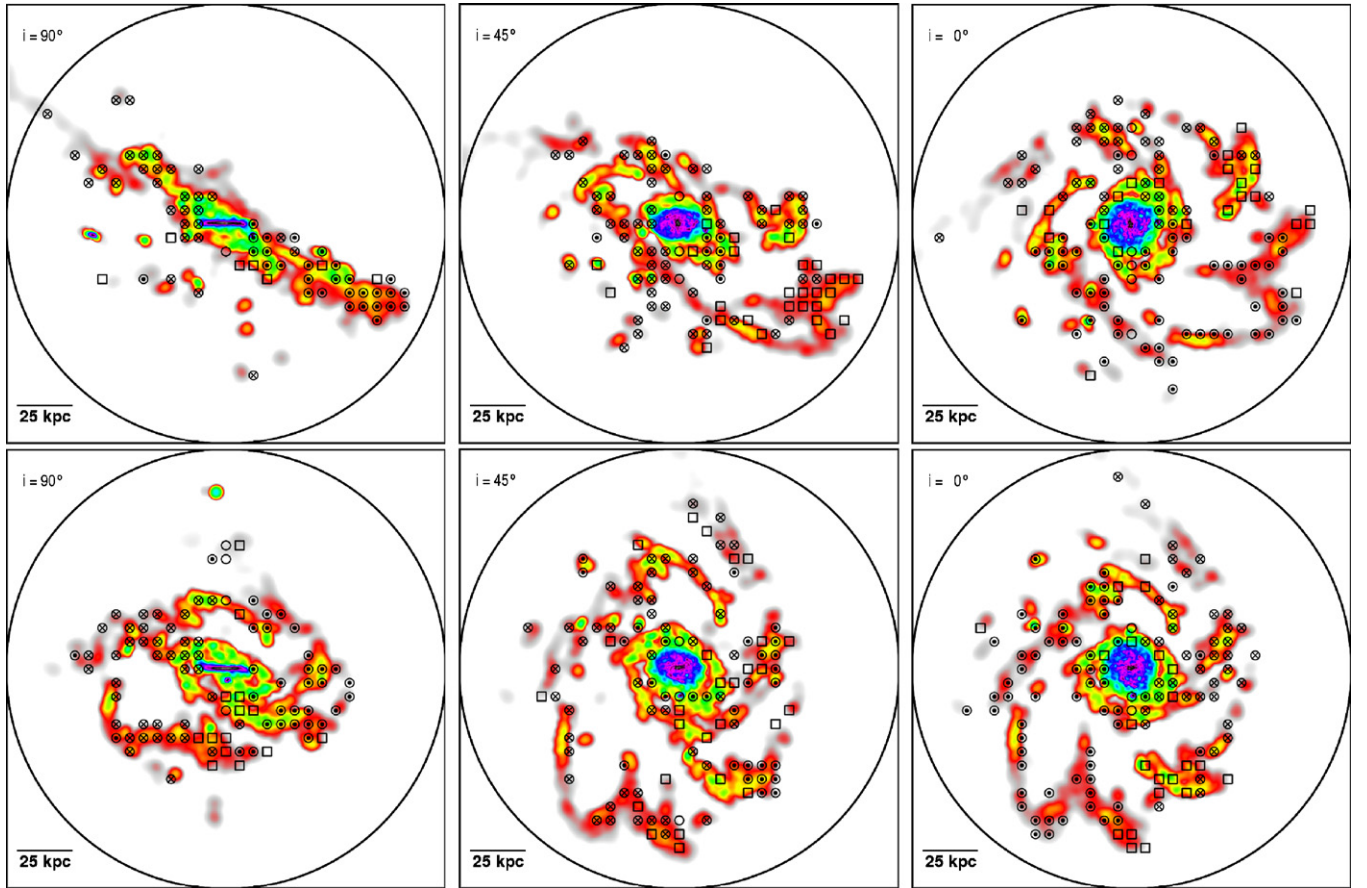


**Figure 8.** Identical to Figure 6, but showing the effect of galaxy inclination on the co-rotation signature. The left, middle, and right panels show galaxy inclinations of  $90^\circ$ ,  $45^\circ$ , and  $0^\circ$ , such that the right panels are top-down views of the left panels. The top and bottom panels represent different angles around the galaxy (at fixed inclination,  $90^\circ$  apart). Note from the top left panel that most of the cool co-rotating halo gas is in an extended warped disk structure. Due to projection effects, gas that is co-rotating in this extended disk appears to be anti-rotating when the galaxy is near face-on.

(A color version of this figure is available in the online journal.)

plane: a warped disk of cool accreted gas that extends to a radius of  $\sim 50\text{--}75$  co-moving kpc (not an unusual occurrence in hydrodynamic simulations; e.g., Agertz et al. 2009; Roškar et al. 2010). These structures, which we choose to call *cold flow disks*, contribute a significant portion of the total cool halo gas in our galaxies and tend to align roughly with the large-scale inflow filaments (see Figure 1). Cold flow disks tend to be common and prolonged phenomena in our simulations, and will arise naturally in systems with the high specific angular momentum content we measure.

The top left panel demonstrates that the cold flow disk is, in fact, co-rotating with the galaxy, since the vast majority of absorption sight lines show co-rotation (circle-X on the left, circle-dot on the right); i.e., the warped disk is rotating in roughly the same manner as the galaxy. Now consider the projection effects of viewing this same galaxy from the top down. Because the left side of the gaseous disk is now projected out of the image, and the right side of the gaseous disk is projected into the image, the top half of the image is blueshifted, and the bottom half is redshifted. Even though the gaseous disk is co-rotating with the galaxy, the warp of the extended disk, in combination with projection effects result in a perceived co-rotation fraction of  $\sim 50\%$  when the galaxy is near face-on.

The bottom panels show an even more severe example of projection effects. In the left image, the warped disk is now seen in projection along the image, into the image along the top half and out of the image along the bottom half. Again, the

co-rotation signature is evident, with the left side of the warped disk being redshifted and the right side blueshifted, the same as the galaxy. Once this image is viewed face-on (bottom right panel), the projected warp of the disk has completely flipped; the top half is now projecting out of the image, and bottom half is projecting into the image. As a result, the line-of-sight velocity of the gas changes sign as well, and the entire warped disk appears to anti-rotate with the galaxy.

As evidenced by these examples, projected co-rotation of cool halo gas via absorption is not a reliable indicator of true co-rotation unless the galaxy is viewed near edge-on. Even if 100% of cool halo gas is in rough co-rotation with the galaxy's disk (e.g., in a cold flow disk), absorption lines around moderately face-on galaxies may give false impressions of anti-rotation.

## 5. EVOLUTION OF THE ORBITING AND CO-ROTATING SIGNATURES

In Section 4, we focused on a single example: Halo 2 at  $z = 1.4$ . For this galaxy at this particular point in time, we found an overwhelming signature of orbiting gas (cool gas completely offset from the systemic velocity if viewed in absorption) and co-rotating gas (cool gas rotating in the same direction as the galactic disk when viewed in absorption), using mock absorption profiles along lines of sight through the galaxy halo. Our goal has been to aid direct comparison to observations that utilize metal line absorption along lines of sight to background quasars. We

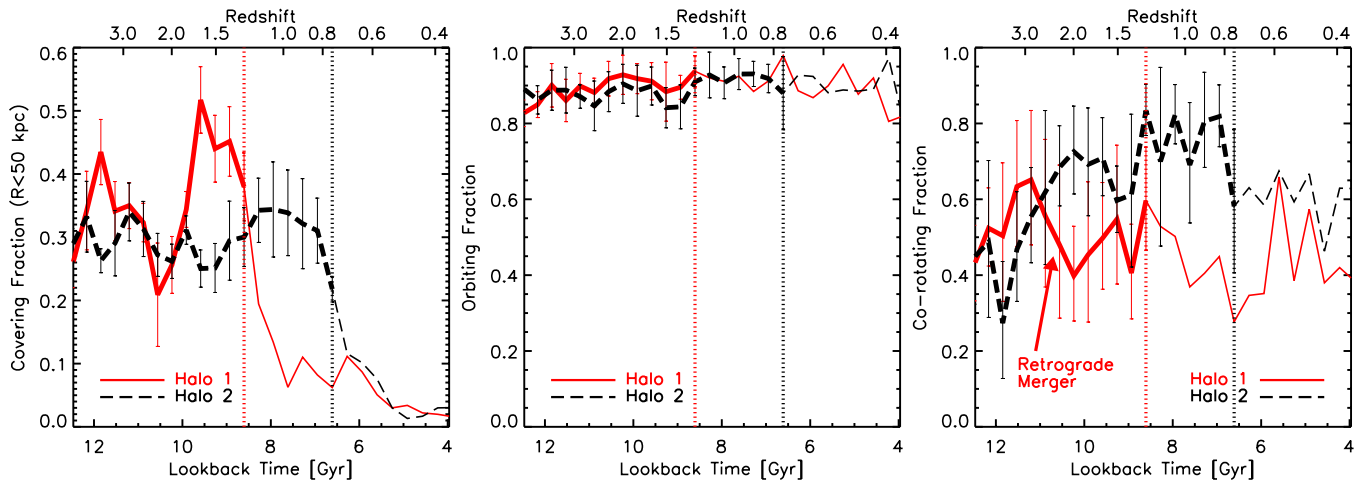


**Figure 9.** Covering fraction, orbiting fraction, and co-rotation fraction vs. time for both simulated galaxies, when viewed near edge-on (inclination  $> 70^\circ$ ). The solid and dashed curves are for Halo 1 and Halo 2, respectively. The error bars show the  $1\sigma$  scatter about the mean when averaging over 12 different viewing angles (see the text).

(A color version of this figure is available in the online journal.)

now repeat our kinematic analysis for both simulations, and at a variety of redshifts, in order to determine if our previous example was an unusual case, or if it points to a predictable signature in the behavior of cool accreted halo gas in galaxies. Because we found that projection effects result in unreliable rotation signatures unless the galaxy is viewed near edge-on (in regard to co-rotation versus anti-rotation; see Section 4.2), we now limit our analysis to inclinations of  $i \geq 70^\circ$ .

Figure 9 shows the covering fraction (left panel), orbiting fraction (middle panel), and co-rotating fraction (right panel) of Halo 1 (solid red lines) and Halo 2 (dashed black lines) for sight lines within  $R < 100$  co-moving kpc, and with  $N_{\text{H I}} > 10^{16} \text{ cm}^{-2}$ . Error bars show the  $\sigma$  scatter due to different galaxy orientations, as discussed in Section 4.2. In the right two panels, the curves change from thick to thin (and we discontinue error bars) when the galaxy transitions from cold-mode accretion to hot-mode accretion (see Section 6.3 for more discussion of this transition). After this transition, the covering fraction of absorption gas drops precipitously (as seen in the left panel), resulting in small number statistics and large error bars. We also note that the total mass in cool halo gas drops significantly after this transition as well (Figure 4) and our galaxies evolve into more bulge-dominated systems (due to major mergers and secular processes, combined with the lack of a reservoir of cool high angular momentum halo gas) making the very definition of co-rotation with a presumed galactic disk nonsensical. Though not shown in this figure (for clarity), we find that the results in the two right panels are nearly identical for sight lines within  $R < 50$  co-moving kpc (as opposed to  $R < 100$ ), indicating a very weak dependence on radius, if any.

Although our statistics are limited to a single pair of simulated galaxies, the middle panel of Figure 9 suggests that very high orbiting fractions ( $\sim 80\%–95\%$ ) may be a natural consequence of cosmological gas accretion in LCDM, even for galaxies with quite different merger histories, such as our two galaxies. The co-rotation fraction, though, shows distinct differences between our two galaxies. Halo 2 experiences a quiescent merger history at  $z > 0.8$ , and shows a very strong signature of co-rotation once it builds a stable disk galaxy at its center ( $\sim 60\%–80\%$  of all sight lines for  $z \lesssim 2.5$ ). Halo 1 has a similar accretion history (and co-rotation fraction evolution) until  $z \sim 2.7$ , at which point it experiences a quick succession of two large mergers at  $z \sim 2.3$ .

While mergers at high redshift are commonplace, the infall trajectory of the merger at  $z \sim 2.3$  is strongly misaligned with the overall rotation of the galaxy (and halo) at that time. As a result, this merger completely re-orientates the angular momentum axis of the galaxy, so that Halo 1’s galaxy at  $z = 1.5$  is rotating in the opposite direction as its progenitor at  $z = 2.5$ . Without knowing how often major mergers result in such a drastic redistribution of angular momentum, it is impossible to speculate on how representative Halo 1 is, in terms of the kinematics of its cool halo gas between  $z \sim 1.5–2.5$ . Even in this severe case, with the angular momentum axis of the galaxy changing drastically due to a large retrograde merger, if we disregard a brief transition period near  $z = 2$ , Halo 1 still shows an average co-rotation fraction of  $\sim 50\%–60\%$  of all sight lines.

## 6. OBSERVATIONAL IMPLICATIONS

### 6.1. Accretion Signature versus Outflows

Summarizing our results from Section 5, we find that  $\sim 80\%–95\%$  of absorption sight lines in our simulated galaxies orbit about the central galaxy, with significant velocity offsets from systemic. The co-rotation fraction of all sight lines varies in our two galaxies, based on their merger histories, from  $\sim 50\%–60\%$  for Halo 1 to  $\sim 60\%–80\%$  for Halo 2 ( $z < 2.5$ ). Although our lack of radiation transfer may result in quantitative changes to these results, the qualitative kinematic behavior of our galaxies’ cool gaseous halos appears independent of column density. As such, the orbiting and co-rotating signatures we have presented here should be observable via halo absorption systems. We note, however, that since the co-rotation signature requires galaxy kinematic and inclination information, this signature is less useful for high-redshift observations, where such information is difficult (if not impossible) to acquire.

Given the large amount of angular momentum associated with the accreted gas in our simulations, it is hard to imagine a scenario where radial/bi-conical outflows from galactic disks would show such strong orbiting signatures. In principle, gas rotating in the disk could be blown directly upward. In the absence of angular momentum robbing interactions with the ambient hot-halo gas, this gas would preserve a sense of rotation in near-polar projections from the disk. However, the near-polar projection is precisely where infalling gas is least likely to



show velocity offsets. One would expect these outflows to be detected along precisely those projections where infalling gas is least likely to show velocity offsets—where the co-rotating signature is most affected by projection effects for a near edge-on disk—near perpendicular to the plane of the galaxy. Of course, perfectly polar sight lines in such a scenario would also show two-sided velocity peaks (or a broadened peak about zero). This is again quite different from the signature expected from accreted gas.

Moving away from the poles, the expected signal for rotating accreted gas is that a large fraction of the sight lines within  $\sim 45^\circ$  of the disk plane should show velocity offsets of  $\sim 80 \text{ km s}^{-1}$  or more at projected distances of 100 co-moving kpc (40 physical kpc at  $z = 1.5$ ) from the galaxy (see Figure 9). Consider gas that initially samples the angular momentum in a disk rotating at  $\sim 200 \text{ km s}^{-1}$  and with a half-mass radius of  $\sim 5 \text{ kpc}$ . If that gas were blown out to projected radii of 40 kpc without losing any angular momentum to hot-gas halo interactions, we would expect typical velocities of only  $\sim 25 \text{ km s}^{-1}$ , which is significantly smaller than what can be expected for the accreted gas. Furthermore, this estimate may be considered maximal in the sense that outflows are expected to preferentially expel low angular momentum material from galaxies, rather than ejecting disk gas that uniformly samples velocities within the disk (Maller & Dekel 2002; Brook et al. 2011).

One possible concern is that the inclusion of outflowing gas may radically disrupt the behavior of the accreted gas, such that it no longer shows a clear signature of orbiting/co-rotating about the galaxy. While it is beyond the scope of this paper to investigate the effects of outflows on cold-mode gas accretion, a recent study by Brook et al. (2011) found that while outflowing gas in their simulations (which tended to be bi-conical, near perpendicular to the disk) had a noticeable impact on the overall dynamics of their galaxies, the high angular momentum extended gas disks were least affected by the outflowing gas, since these extended disks are (roughly) in the plane of the disk and outflowing material is blown perpendicular to the disk.

## 6.2. Galaxy–Absorber Kinematics

In order to compare our findings to observations, we combine results from several metal line absorption studies that compare the kinematics of the galaxy–absorber pairs (Steidel et al. 2002; Ellison et al. 2003; Chen et al. 2005; Kacprzak et al. 2010). The redshift range for the total combined sample is  $0.1 < z < 1.0$ , with typical projected radii  $R \sim 20\text{--}100$  physical kpc between the galaxy and the absorber, and typical galaxy luminosities of  $\sim 0.6 L^*$ . While our simulated galaxies grow too massive at  $z \lesssim 1$  to make a direct comparison in the same redshift interval (their cold-mode accretion ends, and they quickly lose their cool gaseous halos) our galaxies are of comparable luminosity  $\sim 0.4 L^*$  at  $z > 1$ . While we urge the reader to keep this redshift discrepancy in mind, we believe a useful comparison can still be made, since the covering fraction of infalling cool gas appears to be more strongly correlated with halo mass than redshift (see Figure 9; also see Stewart et al. 2011).

Limiting these observations to galaxies with disk-like morphology (and not counting repeat analysis of the same object), these four studies contain (5, 1, 3, and 10) unique pairs of objects, respectively. Adopting our same definitions of orbiting and co-rotating sight lines as defined in Section 2.2, we find that (4, 1, 2, and 7) of these absorbers are orbiting, with an observed orbiting fraction of 74% (14/19).

**Table 1**  
Orbiting and Co-rotating Signatures: Simulations versus Observations

	Observations <sup>a</sup>	Halo 1	Halo 2
Redshift range	0.1–1.0	1.3–2.5	0.8–2.5
Orbiting	74% $\pm$ 20%	80%–95%	80%–95%
Co-rotating	56% $\pm$ 18%	50%–60%	60%–80%

**Note.** <sup>a</sup> Combined sample of Steidel et al. (2002), Ellison et al. (2003), Chen et al. (2005), and Kacprzak et al. (2010).

Of the 14 orbiting systems from this combined sample, (1, 0, 0, and 1) systems were at a near right angle to the galactic disk. These ambiguous systems are removed from further comparison. Classifying the remaining 12 systems, we find that (3, 1, 2, and 3) showed co-rotation, with only (0, 0, 0, and 3) showing anti-rotation. This suggests that roughly 75% (9/12) of orbiting systems are co-rotating, for a total co-rotation fraction of 56%. A summary comparison of these observed values to our simulations is shown in Table 1, including Poisson  $\sqrt{N}$  errors on the total number of galaxy–absorber pairs used to compute each statistic. In general, we find that these observations are in very good agreement with our predicted values, suggesting that these absorption studies may constitute the first indirect observations of cosmological gas accretion onto galaxies. Indeed, a comparison to cosmological simulations was part of the analysis of Kacprzak et al. (2010). They concluded that the absorption systems were consistent with the properties of cosmologically infalling gas in LCDM.

We also compare to Kacprzak et al. (2011), who performed a similar analysis for a sample of absorber–galaxy pairs around more massive galaxies at  $z \sim 0.1$  for more luminous galaxies  $\sim 1.9 L^*$ . Only 54% (7/13) of sight lines in this sample orbit the galaxies.<sup>18</sup> The lower orbiting fraction suggests that these absorption systems show more complex kinematics than freshly accreted gas, though the analysis of Kacprzak et al. (2011) suggests that they are not well fit by purely outflowing gas, either. For purposes of co-rotation versus anti-rotation, we remove from their sample two absorption lines near perpendicular to the slit across galaxy, as well as two sight lines around elliptical galaxies that are not dominated by ordered rotation. Of this modified sample (which contains three orbiting systems) only one sight line shows co-rotation with the galaxy.

This co-rotation fraction is slightly lower than expected for galaxies above the critical transition mass for shock-heating infalling gas, though the qualitative trend agrees with our findings. Indeed, their sample consists of galaxies with Sloan Digital Sky Survey  $M_r$  magnitudes in the range (−20 to −21), appropriate for those inhabiting dark matter halos with masses that span the transition mass  $M_{\text{vir}} \sim 10^{12} M_\odot$  (see, e.g., Tollerud et al. 2011). Unlike the less massive, higher redshift samples (Kacprzak et al. 2010, as well as Steidel, Ellison, Chen, and collaborators) the massive, low- $z$  galaxies of Kacprzak et al. (2011) are *not expected* to have halos dominated by freshly accreted (and orbiting) cold-mode gas. The paucity of cold-mode accretion for massive galaxies means that the cool gas present in these systems is more likely to be the result of outflow material which should not display the co-rotation signatures outlined in this paper. Alternately (unless it is associated with

<sup>18</sup> Kacprzak et al. (2011) quotes a velocity-offset fraction of 5/13, rather than 7/13, because two of their galaxies have *most* of their absorption offset to one side, but not all. We include these two cases as orbiting for the sake of this comparison, but neither definition changes our qualitative conclusions here.

visible infalling satellite galaxies), cool gas in these massive galaxies may also be the result of cloud condensation from the hot halo, which is roughly equally likely to be co-rotating or anti-rotating (see the right panel of Figure 9, after the shock-heating transition). The analysis of Kacprzak et al. (2011) suggests that the systems observed are not likely to be environmental galaxy–galaxy effects, or from star-formation-driven winds, making gas accretion from the hot halo the most likely option for this sample.

### 6.3. Covering Fractions

So long as galaxies experience cold-mode accretion, infalling gas results in moderate covering fractions in the inner halos of these galaxies (Faucher-Giguere & Keres 2011; Kimm et al. 2011; Fumagalli et al. 2011), though the resulting covering fractions are smaller than observed for high redshift galaxies dominated by signatures of outflows (e.g., Steidel et al. 2010). In a previous work (Stewart et al. 2011), we examined the covering fraction as a function of halo mass for the same two simulated galaxies studied in this paper, finding that once each galaxy crosses a critical threshold in halo mass,  $M_{\text{vir}} \sim 10^{12} M_{\odot}$ , almost no cool accreted gas reaches the inner region of the halo. The underlying cause for this transition is because beyond a certain mass halos are capable of sustaining shocks in infalling gas, allowing the vast majority of cool accreted gas to shock heat (see, e.g., Birnboim & Dekel 2003; Kereš et al. 2005; Dekel & Birnboim 2006; Kereš et al. 2009b; Faucher-Giguere et al. 2011; van de Voort et al. 2011).<sup>19</sup> As a result, Stewart et al. (2011) found a strong trend between the covering fraction of cool halo gas and halo mass;  $f_c(< 50 \text{ co-moving kpc}) \sim 30\%–50\%$  before this transition, and only  $\sim 5\%$  afterward. This sharp decline in covering fraction afterward is also shown in the left panel of Figure 9.

This transition in covering fraction should be observable in absorption studies, provided there is some way to distinguish accreted gas from other sources of cool halo gas (e.g., outflows from the galaxy). The results we have presented here allow observations to do precisely this. For any given absorption line through a galaxy’s gaseous halo, cosmologically accreted cool gas should almost always orbit about the galaxy (orbiting fraction of 80%–95%), and most sight lines should be co-rotating with the nearest side of the galactic disk, as long as the galaxy is viewed near edge-on (co-rotation fraction  $\sim 60\%–70\%$ ).

Coupling the results of this paper with those of Stewart et al. (2011), we predict a clear, observable signature in the kinematics of galaxy–absorber pairs as a function of halo mass. Below the critical halo mass, some portion of the cool halo gas detected in absorption will be due to cool accreted gas.<sup>20</sup> *This accreted gas will co-rotate with the galaxy.*

Above the critical halo mass, cool accreted gas no longer contributes substantially to the covering fraction, so even if the total covering fraction remains high (as a result of outflows) the absorbing gas will no longer co-rotate. As a result, *the covering fraction of co-rotating sight lines should drop dramatically at or near this critical halo mass.* While current observations lack the statistical power and halo mass range to robustly test this

prediction, we believe that future observations that continue to compare the properties of many absorption systems with their associated galaxies will be vital in furthering our understanding of gas accretion onto galaxies, as well as the nature of gaseous halos around galaxies.

### 6.4. Connections with Extended UV and H I Disks

The extended cold flow disk structures visualized in Figure 8 may help explain the existence of extended UV disks (Thilker et al. 2005, 2007), large H I disks (García-Ruiz et al. 2002; Oosterloo et al. 2007; Walter et al. 2008), and some stellar disks (Barth 2007) that extend to  $\sim 50$  kpc (or more in some cases). It is generally hard to understand the existence of disks with radial extents as large as  $\sim 50$  kpc in models that link disk galaxy sizes to *dark matter* spins of  $\lambda_{\text{dm}} \sim 0.04$  (Fall & Efstathiou 1980; Mo et al. 1998; Bullock et al. 2001; Dutton & van den Bosch 2009). In these simple models, disk material is expected to extend to radii  $R_{\text{disk}} \simeq \lambda R_{\text{vir}} = 10$  kpc for galaxy-size halos of virial radius  $R_{\text{vir}} \simeq 250$  kpc. More extended gas disks are easier to understand when they arise from cold-mode accretion with spin parameters as high as  $\lambda \sim 0.2$  (Figure 4). Therefore, we expect extended UV disks and extended H I disk configurations to be more common in halos less massive than  $\sim 10^{12} M_{\odot}$  (or with maximum circular velocities smaller than  $\sim 165 \text{ km s}^{-1}$ ), though a detailed comparison between the cold flow disks simulated here and observed extended UV and extended H I disks is beyond the scope of this work.

### 6.5. High-redshift Limitations

While the high orbiting fractions predicted here for infalling cold-mode gas only requires a systemic velocity for the galaxy, the co-rotation signature has a notable limitation in that it requires detailed galaxy information (rotation curve, morphology, inclination) in order to compare galactic rotation with the associated absorption system. While this is possible for low-redshift galaxies (e.g., the combined sample discussed previously), it is extremely difficult at higher redshifts, making the co-rotation signature increasingly difficult to observe at high- $z$ .

In addition, because we have focused on cool gas in galaxy halos, rather than filamentary gas that is not associated with a particular galaxy/halo, the radial extent of this orbiting gas scales roughly with the galaxy virial radius (this is why we have focused on co-moving coordinates in our analysis). As a result, the radial extent of this infalling gas (found here to be  $\sim 100$  co-moving kpc) corresponds to relatively small physical separations at high- $z$  ( $\sim 50$  and  $\sim 33$  kpc at  $z = 1$  and  $z = 2$ , respectively). Once again, this is an added difficulty in observing this signature at high redshift, as it is difficult to find bright background objects within such small projected separations to foreground galaxies.

## 7. CONCLUSION

We have used two high-resolution cosmological SPH simulations (with star formation and feedback prescriptions that have proven effective in reproducing realistic galaxies at  $z = 0$ ) as a tool for studying the detailed properties of cool gas in galaxy halos. By creating absorption sight lines probing the column density of cool gas in our simulated galaxies, we make predictions that should be comparable to observations, either via metal line absorption or direct detection of H I, though we note that without radiative transfer, the precise values presented here are

<sup>19</sup> The critical halo mass where galaxies *begin* to accrete more hot gas than cool gas is considerably lower. Using this definition, the transition mass is often quoted as  $\sim 10^{11.5} M_{\odot}$ , rather than  $10^{12} M_{\odot}$ .

<sup>20</sup> We note that without knowing the full effects of outflows, it is impossible to say how large a portion of the detectable cool gas halo will come directly from fresh accretion.

less robust than our qualitative findings. Our primary results are summarized as follows.

1. Cosmologically accreted cold-mode gas contains significant angular momentum compared to the dark matter, and orbits about the galactic halo before falling in to build the central disk. The dimensionless spin parameter of cool halo gas is  $\sim 3\text{--}5$  times higher than that of the dark matter, with  $\lambda_{\text{coolgas}} \sim 0.1\text{--}0.2$ . Cold flows clearly supply not just baryonic mass to galaxies, but angular momentum as well.
2. This orbiting cool halo gas should be observable via background object absorption-line studies as lines that are offset from the galaxy's systemic velocity by  $\sim 50\text{--}100 \text{ km s}^{-1}$ . Specifically,  $\sim 80\text{--}95\%$  of sight lines that show absorption ( $N_{\text{H I}} > 10^{16} \text{ cm}^{-2}$ ) are offset from the central galaxy's systemic velocity in a single direction. This high fraction of lines that are "orbiting" seems an unavoidable consequence of cosmological gas accretion onto disk galaxies. It is universal for both simulations, at all epochs, and is independent of the orientation of the galaxy. The orbiting gas consists of accreted cool gas from the cosmic web and subsequently falls in to help build the disk.
3. Much of the orbiting cool halo gas commonly takes the form of a fairly thick, warped, extended disk in both our galaxies. As a result, the fraction of all sight lines that co-rotate with the galactic disk is also relatively high ( $\sim 55\%$  for Halo 1 and  $\sim 70\%$  for Halo 2). This is a unique, observable signature of cosmological gas accretion, since there is no reason to expect outflowing gas to co-rotate in this fashion. We warn that due to line-of-sight projection effects of the warped disk, this co-rotation signature can only be reliably measured if the galaxy is near edge-on ( $i \gtrsim 70^\circ$ ). Less inclined systems may produce false anti-rotation signatures.
4. We compare our orbiting and co-rotating signatures to a combined observational sample of galaxy-absorber pairs for galaxies of similar luminosities (Steidel et al. 2002; Ellison et al. 2003; Chen et al. 2005; Kacprzak et al. 2010), finding rough agreement between our predictions and these observations (Table 1). These studies may provide some of the first (indirect) observational evidence for cosmological accretion of cool gas onto galaxy halos.
5. The covering fraction of cosmologically accreted cool gas within a given radius,  $f_c(< R)$ , is a strong function of  $R$ . At small radii, the covering fraction is near unity, decreases to negligible values at  $R > 100$  co-moving kpc, and is well fit by a power law. The slope of this power law depends on the minimum column density of absorbing gas:  $f_c(N_{\text{H I}}, < R) = (R/R_0)^{-\beta(N_{\text{H I}})}$ , with our galaxies well fit by  $R_0 \sim 10$  co-moving kpc and  $\beta(> 10^{16} \text{ cm}^{-2}) \sim 0.6\text{--}0.8$  (see Equations (1)–(3)).
6. The extended, warped, and thick cold-mode disks illustrated in Figure 8 may be associated with the extended UV and H I disks observed for galaxies in the nearby universe (Thilker et al. 2005, 2007; Oosterloo et al. 2007; Walter et al. 2008). If so, we expect extended disk configurations to be more common for galaxies in halos less massive than  $\sim 10^{12} M_\odot$  (or with maximum circular velocities smaller than  $\sim 165 \text{ km s}^{-1}$ ). We note that H I and extended UV disks as large as those sometimes seen ( $\sim 50$  kpc) are quite difficult to understand if the available angular momentum for the gas mirrors that in the dark matter, as is often assumed in simple LCDM-based models of disk formation (e.g., Fall & Efstathiou 1980; Bullock et al. 2001; Dutton & van den Bosch 2009, where  $R_{\text{disk}} \simeq \lambda R_{\text{vir}}$  and  $\lambda \sim 0.04$ ).

If these disks are instead supported by cold accreted material (with  $\lambda \sim 0.1\text{--}0.2$ ) their extent and structure are more naturally explained.

Our expectation is that cold-mode accretion will result in circumgalactic gas that orbits with fairly high angular momentum. Spherical outflows will be characteristically radial with low angular momentum, in stark contrast to infalling gas. While bi-conical outflows may give velocity offsets under certain projections, similar to the accretion signature discussed here, the resulting outflows will exhibit primarily polar configurations; this is precisely where infalling gas is less likely to show velocity offsets and the orbiting/co-rotating signature is least reliable. Given a sufficiently large sample of galaxy-absorber pairs, it should be possible to determine the fraction of orbiting and non-orbiting halo gas as a function of host halo mass, and to test the expectation that less massive halos (below the critical shock mass) should preferentially host a higher fraction of cold-mode/orbiting gas than their more massive counterparts.

We thank Leonidas Moustakas and David Weinberg for useful discussions. We thank the anonymous referee, whose insightful comments helped improve the quality of this paper. The simulations used in this paper were run on the Cosmos cluster at JPL and the Greenplanet cluster at UC Irvine. This research was carried out at the Jet Propulsion Laboratory, California Institute of Technology, under a contract with the National Aeronautics and Space Administration. J.S.B. and K.R.S. were partially supported by NASA grant NNX09AG01G. K.R.S. is supported by an appointment to the NASA Postdoctoral Program at the Jet Propulsion Laboratory, administered by Oak Ridge Associated Universities through a contract with NASA. T.K. and J.D. have been supported by the Swiss National Science Foundation (SNF).

## REFERENCES

- Abel, T., Anninos, P., Zhang, Y., & Norman, M. L. 1997, *New Astron.*, **2**, 181  
 Agertz, O., Teyssier, R., & Moore, B. 2009, *MNRAS*, **397**, L64  
 Bailin, J., et al. 2005, *ApJ*, **627**, L17  
 Barnes, J., & Efstathiou, G. 1987, *ApJ*, **319**, 575  
 Barth, A. J. 2007, *AJ*, **133**, 1085  
 Behroozi, P. S., Conroy, C., & Wechsler, R. H. 2010, *ApJ*, **717**, 379  
 Berta, Z. K., Jimenez, R., Heavens, A. F., & Panter, B. 2008, *MNRAS*, **391**, 197  
 Bertschinger, E. 2001, *ApJS*, **137**, 1  
 Bett, P., Eke, V., Frenk, C. S., Jenkins, A., Helly, J., & Navarro, J. 2007, *MNRAS*, **376**, 215  
 Bett, P., Eke, V., Frenk, C. S., Jenkins, A., & Okamoto, T. 2010, *MNRAS*, **404**, 1137  
 Binney, J. 1977, *ApJ*, **215**, 483  
 Birnboim, Y., & Dekel, A. 2003, *MNRAS*, **345**, 349  
 Black, J. H. 1981, *MNRAS*, **197**, 553  
 Blumenthal, G. R., Faber, S. M., Flores, R., & Primack, J. R. 1986, *ApJ*, **301**, 27  
 Bond, N. A., Churchill, C. W., Charlton, J. C., & Vogt, S. S. 2001, *ApJ*, **562**, 641  
 Bouché, N., Murphy, M. T., Péroux, C., Csabai, I., & Wild, V. 2006, *MNRAS*, **371**, 495  
 Boylan-Kolchin, M., Ma, C.-P., & Quataert, E. 2008, *MNRAS*, **383**, 93  
 Brook, C. B., et al. 2011, *MNRAS*  
 Brooks, A. M., Governato, F., Booth, C. M., Willman, B., Gardner, J. P., Wadsley, J., Stinson, G., & Quinn, T. 2007, *ApJ*, **655**, L17  
 Brooks, A. M., Governato, F., Quinn, T., Brook, C. B., & Wadsley, J. 2009, *ApJ*, **694**, 396  
 Bryan, G. L., & Norman, M. L. 1998, *ApJ*, **495**, 80  
 Bullock, J. S., Dekel, A., Kolatt, T. S., Kravtsov, A. V., Klypin, A. A., Porciani, C., & Primack, J. R. 2001, *ApJ*, **555**, 240  
 Chen, H., Helsby, J. E., Gauthier, J., Shectman, S. A., Thompson, I. B., & Tinker, J. L. 2010, *ApJ*, **714**, 1521  
 Chen, H., Kennicutt, R. C., Jr., & Rauch, M. 2005, *ApJ*, **620**, 703



- Chen, H., & Tinker, J. L. 2008, *ApJ*, **687**, 745
- Churchill, C. W., Mellon, R. R., Charlton, J. C., Jannuzi, B. T., Kirhakos, S., Steidel, C. C., & Schneider, D. P. 2000, *ApJS*, **130**, 91
- Churchill, C., Steidel, C., & Kacprzak, G. 2005, in ASP Conf. Ser. 331, Extra-Planar Gas, ed. R. Braun (San Francisco, CA: ASP), 387
- Dekel, A., & Birnboim, Y. 2006, *MNRAS*, **368**, 2
- Dekel, A., et al. 2009, *Nature*, **457**, 451
- Diemand, J., Kuhlen, M., Madau, P., Zemp, M., Moore, B., Potter, D., & Stadel, J. 2008, *Nature*, **454**, 735
- D'Onghia, E., & Navarro, J. F. 2007, *MNRAS*, **380**, L58
- Dutton, A. A., & van den Bosch, F. C. 2009, *MNRAS*, **396**, 141
- Ellison, S. L., Mallén-Ornelas, G., & Sawicki, M. 2003, *ApJ*, **589**, 709
- Fall, S. M., & Efstathiou, G. 1980, *MNRAS*, **193**, 189
- Faucher-Giguere, C., & Keres, D. 2011, *MNRAS*, **412**, L118
- Faucher-Giguere, C., Keres, D., & Ma, C. 2011, *MNRAS*, submitted (arXiv:1103.0001)
- Fumagalli, M., Prochaska, J. X., Kasen, D., Dekel, A., Ceverino, D., & Primack, J. R. 2011, *MNRAS*, submitted (arXiv:1103.2130)
- García-Ruiz, I., Sancisi, R., & Kuijken, K. 2002, *A&A*, **394**, 769
- Governato, F., Willman, B., Mayer, L., Brooks, A., Stinson, G., Valenzuela, O., Wadsley, J., & Quinn, T. 2007, *MNRAS*, **374**, 1479
- Governato, F., et al. 2009, *MNRAS*, **398**, 312
- Governato, F., et al. 2010, *Nature*, **463**, 203
- Guo, Q., White, S., Li, C., & Boylan-Kolchin, M. 2010, *MNRAS*, **404**, 1111
- Haardt, F., & Madau, P. 1996, *ApJ*, **461**, 20
- Hopkins, A. M., & Beacom, J. F. 2006, *ApJ*, **651**, 142
- Kacprzak, G. G., Churchill, C. W., Barton, E. J., & Cooke, J. 2011, *ApJ*, **733**, 105
- Kacprzak, G. G., Churchill, C. W., Ceverino, D., Steidel, C. C., Klypin, A., & Murphy, M. T. 2010, *ApJ*, **711**, 533
- Kacprzak, G. G., Churchill, C. W., Steidel, C. C., Murphy, M. T., & Evans, J. L. 2007, *ApJ*, **662**, 909
- Katz, N., Weinberg, D. H., & Hernquist, L. 1996, *ApJS*, **105**, 19
- Kereš, D., & Hernquist, L. 2009, *ApJ*, **700**, L1
- Kereš, D., Katz, N., Davé, R., Fardal, M., & Weinberg, D. H. 2009a, *MNRAS*, **396**, 2332
- Kereš, D., Katz, N., Fardal, M., Davé, R., & Weinberg, D. H. 2009b, *MNRAS*, **395**, 160
- Kereš, D., Katz, N., Weinberg, D. H., & Davé, R. 2005, *MNRAS*, **363**, 2
- Kimm, T., Slyz, A., Devriendt, J., & Pichon, C. 2011, *MNRAS*, **413**, L51
- Macciò, A. V., Dutton, A. A., van den Bosch, F. C., Moore, B., Potter, D., & Stadel, J. 2007, *MNRAS*, **378**, 55
- Maller, A. H., & Bullock, J. S. 2004, *MNRAS*, **355**, 694
- Maller, A. H., & Dekel, A. 2002, *MNRAS*, **335**, 487
- Maller, A. H., Dekel, A., & Somerville, R. 2002, *MNRAS*, **329**, 423
- Martin, C. L. 2005, *ApJ*, **621**, 227
- Martin, C. L., & Bouché, N. 2009, *ApJ*, **703**, 1394
- Mo, H. J., Mao, S., & White, S. D. M. 1998, *MNRAS*, **295**, 319
- Oosterloo, T. A., Morganti, R., Sadler, E. M., van der Hulst, T., & Serra, P. 2007, *A&A*, **465**, 787
- Peebles, P. J. E. 1969, *ApJ*, **155**, 393
- Pontzen, A., et al. 2008, *MNRAS*, **390**, 1349
- Prochter, G. E., Prochaska, J. X., & Burles, S. M. 2006, *ApJ*, **639**, 766
- Rigby, J. R., Charlton, J. C., & Churchill, C. W. 2002, *ApJ*, **565**, 743
- Roškar, R., Debattista, V. P., Brooks, A. M., Quinn, T. R., Brook, C. B., Governato, F., Dalcanton, J. J., & Wadsley, J. 2010, *MNRAS*, **408**, 783
- Rubin, K. H. R., Prochaska, J. X., Koo, D. C., Phillips, A. C., & Weiner, B. J. 2010, *ApJ*, **712**, 574
- Rubin, K. H. R., Prochaska, J. X., Ménard, B., Murray, N., Kasen, D., Koo, D. C., & Phillips, A. C. 2011, *ApJ*, **728**, 55
- Shapley, A. E., Steidel, C. C., Pettini, M., & Adelberger, K. L. 2003, *ApJ*, **588**, 65
- Sharma, S., & Steinmetz, M. 2005, *ApJ*, **628**, 21
- Shen, S., Wadsley, J., & Stinson, G. 2010, *MNRAS*, **407**, 1581
- Silk, J. 1977, *ApJ*, **211**, 638
- Spergel, D. N., et al. 2007, *ApJS*, **170**, 377
- Stadel, J. G. 2001, PhD thesis, Univ. Washington
- Steidel, C. C. 1995, in Proc. ESO Workshop, QSO Absorption Lines, ed. G. Meylan (Berlin: Springer), 139
- Steidel, C. C., Erb, D. K., Shapley, A. E., Pettini, M., Reddy, N., Bogosavljević, M., Rudie, G. C., & Rakic, O. 2010, *ApJ*, **717**, 289
- Steidel, C. C., Giallisco, M., Pettini, M., Dickinson, M., & Adelberger, K. L. 1996, *ApJ*, **462**, L17
- Steidel, C. C., Kollmeier, J. A., Shapley, A. E., Churchill, C. W., Dickinson, M., & Pettini, M. 2002, *ApJ*, **570**, 526
- Stewart, K. R., Bullock, J. S., Barton, E. J., & Wechsler, R. H. 2009a, *ApJ*, **702**, 1005
- Stewart, K. R., Bullock, J. S., Wechsler, R. H., & Maller, A. H. 2009b, *ApJ*, **702**, 307
- Stewart, K. R., Bullock, J. S., Wechsler, R. H., Maller, A. H., & Zentner, A. R. 2008, *ApJ*, **683**, 597
- Stewart, K. R., Kaufmann, T., Bullock, S., Barton, E., Maller, A., Diemand, J., & Wadsley, J. 2011, *ApJ*, **735**, L1
- Stinson, G., Seth, A., Katz, N., Wadsley, J., Governato, F., & Quinn, T. 2006, *MNRAS*, **373**, 1074
- Thilker, D. A., et al. 2005, *ApJ*, **619**, L79
- Thilker, D. A., et al. 2007, *ApJS*, **173**, 538
- Tinker, J. L., & Chen, H. 2008, *ApJ*, **679**, 1218
- Tollerud, E. J., Bullock, J. S., Graves, G. J., & Wolf, J. 2011, *ApJ*, **726**, 108
- van den Bosch, F. C., Abel, T., Croft, R. A. C., Hernquist, L., & White, S. D. M. 2002, *ApJ*, **576**, 21
- van de Voort, F., Schaye, J., Booth, C. M., & Dalla Vecchia, C. 2011, *MNRAS*
- Verner, D. A., & Ferland, G. J. 1996, *ApJS*, **103**, 467
- Vitvitska, M., Klypin, A. A., Kravtsov, A. V., Wechsler, R. H., Primack, J. R., & Bullock, J. S. 2002, *ApJ*, **581**, 799
- Wadsley, J., et al. 2004, *New Astron.*, **9**, 137
- Walter, F., Brinks, E., de Blok, W. J. G., Bigiel, F., Kennicutt, R. C., Thornley, M. D., & Leroy, A. 2008, *AJ*, **136**, 2563
- Weiner, B. J., et al. 2009, *ApJ*, **692**, 187
- Weinmann, S. M., Kauffmann, G., van den Bosch, F. C., Pasquali, A., McIntosh, D. H., Mo, H., Yang, X., & Guo, Y. 2009, *MNRAS*, **394**, 1213
- White, S. D. M., & Frenk, C. S. 1991, *ApJ*, **379**, 52
- White, S. D. M., & Rees, M. J. 1978, *MNRAS*, **183**, 341